The heterogeneous band microstructure and mechanical performance in a wire + arc additively manufactured 2219 Al alloy

Yinghui Zhou[a,b], Xin Lin[a,b*], Nan Kang [a,c*], Yao Tang [a,b], Weidong Huang [a,b] , Zhennan Wang[a,b]

a: State Key Laboratory of Solidification Processing, Northwestern Polytechnical University, Xi'an, Shaanxi, 710072, PR China

b: Key Laboratory of Metal High Performance Additive Manufacturing and Innovative Design, MIIT China, Northwestern Polytechnical University, Xi'an,Shaanxi 710072, PR China

c: Arts et Metiers Institute of Technology, MSMP, HESAM Université, F-51006 Châlons-en-Champagne, France

**corresponding authors*

State Key Laboratory of Solidification Processing,

Northwestern Polytechnical University,

Xi'an Shaanxi 710072, PR China

E-mail address: xlin@nwpu.edu.cn (Xin Lin)

nan.kang@ensam.eu (Nan KANG).

[*]Corresponding author.

E-mail address: xlin@nwpu.edu.cn (X. Lin).

Abbreviations. AC: air-cooled; AM: additive manufacturing; CET: columnar–equiaxed grain transition; CT: computed tomography; DIC: digital image correlation; EBSD: electron backscatter diffraction; EL: elongation; FIB: focused ion beam; GND: geometrically necessary dislocation; GTAW: gas tungsten arc welding; HADDF: high-angle annular dark field; HRTEM: high-resolution transmission electron microscopy; IPF: inverse pole figure; PDAS: primary dendrite arm spacing; PLC: Portevin–Le Chatelier; SEAD: selected electron area diffraction; SEM: scanning electron microscope; SLM: selective laser melting; STEM: scanning transmission electron microscopy; TEM: transmission electron microscope; UTS: ultimate tensile strength; WAAM: wire + arc additive manufacturing; WC: water-cooled; YS: yield strength.

Abstract

In this study, a 2219 Al alloy with a heterogeneous band structure characterized by an alternating distribution of equiaxed and columnar α-Al grains was obtained by wire + arc additive manufacturing. The volume fractions of the equiaxed and columnar grains were varied by adjusting the cooling mode of the substrate. The volume fraction of the columnar grains in a water-cooled (WC) deposit was approximately 16% higher than that in an air-cooled (AC) deposit. Moreover, the WC deposit exhibited smaller primary arm dendrite spacing and lower porosity than those of the AC deposit. The results of *in-situ* tensile testing revealed that the columnar grains could coordinate and distribute strain more effectively than the equiaxed grains. The *ex-situ* electron back scatter diffraction data showed that the observed deformations of the columnar and equiaxed grains during tensile testing were non-uniform and non-synchronization. Furthermore, numerous dislocations in the columnar grains of the deposit coordinated the deformation process. According to tensile testing data, the ultimate strength, yield strength, and elongation of the WC deposit were 247.7±17.7 MPa, 110.1±6.3 MPa and 11.9±0.7 %, which were higher than those of the AC deposit by 10.76%, 15.78%, and 26.78%, respectively. Therefore, the heterogeneous band structure of the equiaxed and columnar grains ensured good synergy between strength and ductility.

Key words: Wire + arc additive manufacturing; 2219 Al alloy; heterogeneous band microstructure; strength-ductility synergy

1. Introduction

Al-Cu alloys are widely used in the aerospace and automotive fields, owing to their attractive properties such as low density, high strength, high heat resistance, and excellent formability [1]. Wire + arc additive manufacturing (WAAM) technology is a metal additive manufacturing (AM) method that uses an arc as a heat source and welding wire as the deposited material for fabricating large-sized components [2-4]. WAAM can be applied to the large-scale industrial production due to its high forming efficiency and low cost and thus has received much attention from researchers that stimulated its rapid development [5, 6].

To date, WAAM has been successfully applied to the manufacturing of metal components from various Al alloys such as Al-6.3Cu [7-9], Al-6Mg [10], Al-Cu-Mg [11, 12], Al-Mg-4.5Mn [13]. It was reported previously [2, 14] that the WAAM-processed 2219 Al alloy had a typical heterogeneous band microstructure with an alternating distribution of equiaxed α-Al grains in the interlayers and columnar α-Al grains in the inner layers. Generally, solidification conditions strongly affect the grain morphology [15, 16]. A high thermal gradient (G)-to-growth rate (R) ratio results in the formation of an epitaxial columnar grain zone, and a low value G/R value promotes the formation of equiaxed grains in most AM-processed Al alloys [17]. In addition, many studies have shown that the presence of Sc, Zr, and Ti elements can cause the precipitation of Al_3Sc, Al_3Zr, and Al_3Ti particles, thus facilitating the formation of α-Al equiaxed grains through heterogeneous nucleation[18]. In a selective laser melting (SLM)-processed Al-Mg-Sc-Zr alloy, $Al_3(Sc,Zr)$ particles are primarily responsible for the growth of equiaxed grains via heterogeneous nucleation [18, 19]. Yang et al. [20] suggested that the equiaxed grain bands at the melt pool boundaries mainly resulted from the heterogeneous nucleation of α-Al species on the Al_3Zr particles in the remelting zone. Previous studies [21-23] have shown that heterogeneous nucleation particles can exist in a very narrow region near the melting boundary with a temperature range during welding. However, there was a significant difference in the solidification conditions between the SLM and WAAM processes, such as temperature gradient (G),

solidification rate (R), and cooling rate (ε). The G in SLM [24]and WAAM [9, 25]is 10^5-10^6 K/m and 10^4-10^5 K/m, respectively. The R in SLM and WAAM is ~1 m/s and ~10^{-3} m/s, respectively. The cooling rates (~10^6 K/s) encountered during SLM are several orders of magnitude higher than those of WAAM (10^1-10^2 K/s). The differences in solidification conditions during SLM and WAAM lead the difference of G/R, and the CET is also different. The size of the molten pool in WAAM is much larger than that in SLM [26, 27]. Therefore, it is necessary to further systematically study whether the formation reasons for equiaxed and columnar grains in WAAM are consistent with those in SLM and welding requires further investigation.

Grain morphology strongly affects the strength-ductility synergy and anisotropy of materials [28-31]. The isomeric structures of equiaxed and columnar grains in SLM-processed Al alloys have been examined previously, indicating that isomeric structures could simultaneously possess high strength and ductility [32]. However, the sizes of equiaxed and columnar grains in WAAM-processed Al alloys were much larger than those in the SLM-processed Al alloys [33]. Furthermore, the effect of heterogeneous band microstructure on the mechanical properties of these alloys remains unclear. Hence, it is very important to determine the relationship between the heterogeneous microstructure and the strength-ductility synergy in WAAM-processed Al alloys for the successful optimization of their grain structure and mechanical properties.

In this study, a heterogeneous band microstructure with an alternating distribution of equiaxed and columnar α-Al grains was obtained for the WAAM-processed 2219 Al alloy. The volume fractions of the equiaxed and columnar grains were controlled by varying the cooling mode of the substrate. The formation of the heterogeneous microstructure was investigated by performing quantitative simulations. The relationship between the number density of the heterogeneous nucleation sites formed by Al_3Zr particles and solidification conditions was examined. The morphological characteristics of α-Al grains, precipitates and pore defects in the WC and AC deposits were analyzed, and the role of columnar grains in the plastic deformation of these deposits was discussed. The effect of heterogeneous deformation on the strength-ductility synergy was determined by conducting digital image correlation (DIC) tensile,

in-situ tensile, and *ex-situ* electron back scatter diffraction (EBSD) tests. As a result, the relationship between the solidification conditions, heterogeneous microstructure, and mechanical performance of the alloy was established.

2. Experimental methods

2.1 Materials and fabrication procedure

The utilized WAAM system (Figure 1) based on gas tungsten arc welding (GTAW) technology consisted of a 520 A GTAW power supply (EWM Tetrix521), a tungsten inert gas welding torch, and a 4-axis LPM-408 computerized numerical control working table. Table 1 lists the chemical compositions of the ER2319 wire (diameter: 1.2 mm), 2024 Al substrate plate, and WAAM-processed 2219 deposit. The dimensions of the water-cooled substrate were 300 mm×200 mm×10 mm. The utilized deposition parameters are listed in Table 2. In this study, the processed deposit using a water-cooled substrate was defined as a WC deposit, and the processed deposit in an air-cooled environment was defined as an AC deposit. Both deposits contained 30 layers with lengths of 25 cm.

Table 1 The chemical composition of the ER2319 wire, the 2024 substrate, and the WAAM fabricated 2219 Al alloy (wt%.)

Alloys	Cu	Mn	Zr	Ti	Al
Substrate	4.55	0.59	0.01	0.04	Bal.
ER2319	7.25	0.31	0.22	0.14	Bal.
WAAM-processed 2219	6.92	0.31	0.20	0.14	Bal.

Table 2 The deposition parameters used in the WAAM process.

Deposition parameters	Value
Welding Current Type	AC power source
AC power frequency	50 Hz
Wire feed speed (WFS)	2 m/min
Travel Speed (TS)	350 mm/min
Argon	99.99 % purity
Protective gas flow	18 L/min
Stable current (peak/base)	150/100 A
Tungsten electrode diameter	3.2 mm

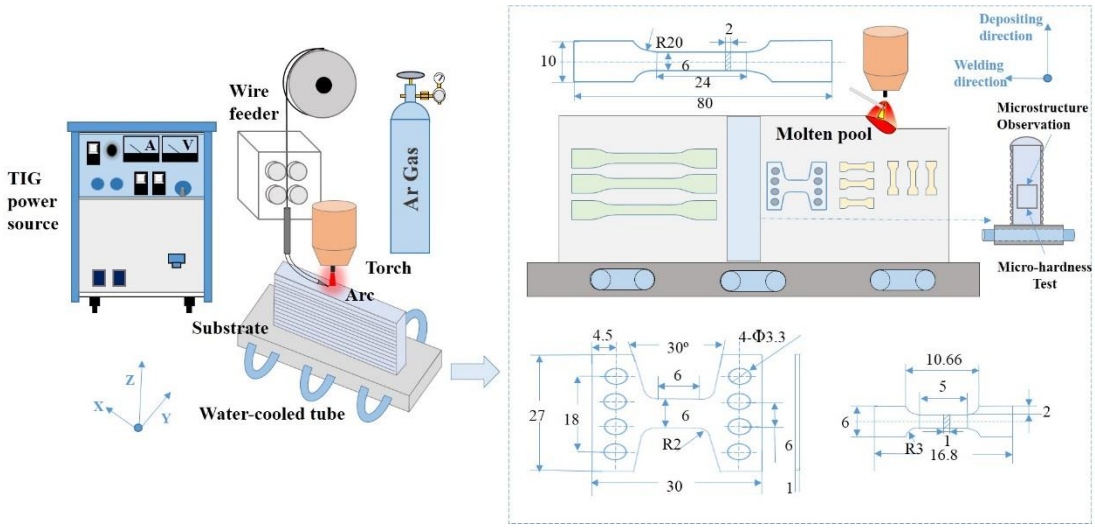

Figure 1 Schematic diagram of the WAAM process as well as the positions and dimensions of the test samples (all size are specified in millimeters).

2.2 Microstructural characterization

The metallographic samples were cut in the middle of the WAAM-processed 2219 Al alloy deposit (Figure 1), ground with sandpaper, polished to a mirror state using a polisher and corroded with Keller′s reagent (2 mL HF, 3 mL HCl, 5 mL HNO_3, and 190 mL H_2O) for 20 s. Grain morphology was observed using an optical microscope (OLYMPUS-GX71), a scanning electron microscope (SEM, Zeiss Gemini 500) equipped with Oxford energy-dispersive X-ray spectroscopy and EBSD modules, and a transmission electron microscope (TEM, FEI, Themis Z) with a double Cs corrector. The crystal orientation of the deposit was analyzed by the Channel 5 software. TEM samples were prepared using a focused ion beam (FIB, FEI Helios G4 CX) technique to accurately select suitable areas in the equiaxed and columnar grain zones of the deposits. High-angle annular dark-field scanning transmission electron microscopy (HADDF–STEM) analysis was performed to characterize precipitates and dislocations. The three-dimensional (3D) morphology of the pores in the deposit structure was examined by a micro-computed tomography (micro-CT) system (ZEISS Xradia 520 Versa), and their volumes and volume fractions were calculated quantitatively using the Dragonfly software. A triangle method was applied to measure the average primary dendrite arm spacing (PDAS) of each sample, as shown in Figure 2 [34-37]. The PDAS

was measured by the distance between the adjacent primary arms of the same orientation in the columnar growth. The cross section of the vertical dendrite primary arms was measured. The adjacent arms were of the same orientation and presented a relatively symmetrical cross shape. The average lengths of the three sides were denoted $\lambda_{1(1)}$, $\lambda_{1(2)}$, and $\lambda_{1(3)}$. These steps were repeated more than five times for different areas of the microstructure to reduce errors. All measurement results were averaged to obtain the PDAS values of the samples.

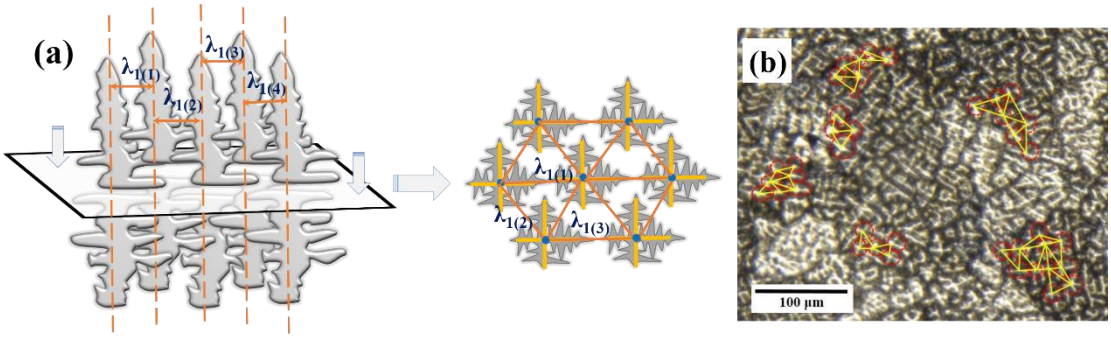

Figure 2 The measuring method of primary dendrite arm spacing:

(a) schematic diagram of triangle method; (b) the experimental measurement

2.3 Mechanical testing

Tensile samples were cut by wire-electrode cutting from the middle zone of the WAAM-processed deposit (Figure 1). Tensile tests were performed on an Instron-3382 testing machine at a strain rate of 1 mm/min. The surface strain of the samples was mapped by DIC during testing. *In-situ* micromechanical tensile experiments were performed using an SEM (Zeiss Gemini 500) equipped with an accessories box for 2- kN EBSD R/T tensile tester, and the real-time microstructural evolution and mechanical response were recorded simultaneously.

2.4 Thermal simulation

Thermal simulation was performed on the ABAQUS software by a Finite Element Method (FEM). The birth and death of element technology were used to simulate the generation of layers [38]. A partial differential equation for the transient heat transfer of the deposit exposed to a volume heat source can be expressed as follows:

$$\rho C_P \frac{dT}{dt} = Q(r,t) - \nabla q(r,t) \quad (1)$$

where ρ is the material density, T is the temperature, C_p is the temperature-dependent specific heat capacity, t is the time, r is the relative reference coordinate, Q is the heat source that depends on location and time, and q is the heat flux that also depends on location and time. The conduction heat flux was computed using Fourier's law as follows:

$$q = -k\nabla T \tag{2}$$

where k is the temperature-dependent thermal conductivity. The convective heat flux is described according to Newton's cooling law:

$$q_{conv} = h_{conv}(T_s - T_\infty) \tag{3}$$

where h_{conv} is the convection heat transfer coefficient, T_s is the deposit surface temperature, and T_∞ is the ambient temperature. The heat flux caused by the heat conduction between the substrate and the clamping system was modeled as follows:

$$q_{cond} = h_{cond}(T_s - T_{clmp}) \tag{4}$$

Where h_{cond} is the heat transfer coefficient by conduction between the two materials in contact, and T_{clmp} is the temperature of the clamping system. The radiation heat flux was calculated according to the Stefan-Boltzmann's law as follows:

$$q_{rad} = \varepsilon_e \sigma(T_s - T_\infty) \tag{5}$$

where σ is the Stefen-Boltzmann constant, and ε_e is the emissivity. The temperature-dependent thermo-physical properties are listed in Table 3. The convection heat transfer coefficient h_{conv}, the emissivity ε_e was set as 20 W/m^2·ºC and 0.21, respectively [37]. The ambient temperature T_∞ for the surfaces except for the bottom surface of the substrate and the temperature of the clamping system T_{clmp} were 25 ºC. The heat loss by the contact conduction through the bottom surface in the simulation case using the common substrate was accounted for by assigning a conduction heat transfer coefficient h_{cond} 80 W/m^2·ºC, while the boundary condition of the bottom surface of the substrate was set to be isothermal with the temperature of the ambient temperature (25 ºC) for the WC substrate. Figure 3 displays the finite-element mesh diagram of the WAAM-processed 2219 Al alloy deposit. The cooling rate and thermal gradient of the

solidification interface in the molten pool of the WAAM process were obtained. The deposition of the single-pass multi-layer 2219 Al alloy was performed in a unidirectional scanning mode. Considering the calculation efficiency and calculation accuracy of the numerical simulation process, the thermal unit of the forming part was set to the DC3D8 (hexahedral eight-node) element with a size of 2.25 mm×2.23 mm× 1.0 mm.

The equilibrium phase diagram of the 2219 Al (Al-6.92Cu-0.32Mn-xZr-0.14Ti (wt.%)) alloy was constructed using the Thermo-Calc 5 software and TTAL7 database (Thermo-Tech Al Database v. 7.1).

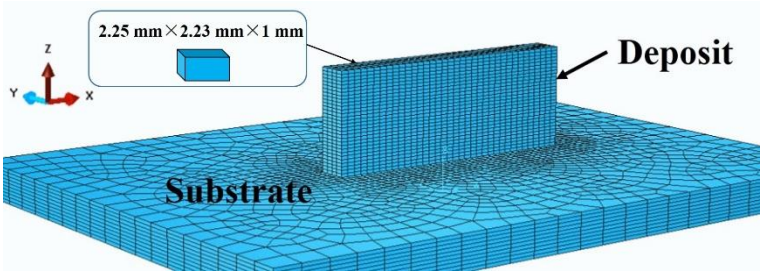

Figure 3 Finite-element mesh of the WAAM-processed 2219 Al alloy.

Table 3 Thermo- physical parameters used in the heat transfer simulation [39].

Property	Unit	T = 25 ℃	T = 820 ℃	T = 930 ℃
Specific heat capacity	J/mol·K	871	871	1060
Thermal conductivity	W/m K	238	238	100
Density	kg/m^3	2700	/	/

3. Results

3.1 Macro and micro structure analysis

Figure 4 shows the microstructure of the WC deposit. They indicate a typical heterogeneous band structure with an alternating distribution of the equiaxed grains in the inter-layer zone and columnar grains in the inner-layer zone. The width of the equiaxed grain band increases from the bottom to the top of the deposit, as shown in Figure 4(a-f). This phenomenon can be attributed to the decreased temperature gradient

and cooling rate along the deposition direction due to heat accumulation. The obtained results indicate that the solidification conditions (temperature gradient and cooling rate) can affect the volume fractions of the equiaxed and columnar grains. Figure 5(a) presents a schematic diagram of microstructure evolution during WAAM process. In this paper, the inner and inter layers are defined according to the macroscopic morphological differences of layers. A complete depositing layer is composed of equiaxed grain zone at the melt pool boundaries and the columnar grain zone at the center. The inter-layer equiaxed grains mentioned in this paper is actually the equiaxed grain zone at the new depositing layer, and the inner-layer region is the columnar grain zone at the middle and upper part of the new depositing layer. The inverse pole figure (IPF) in Figure 5(b) indicates the growth sequence and features from the equiaxed to columnar grains.

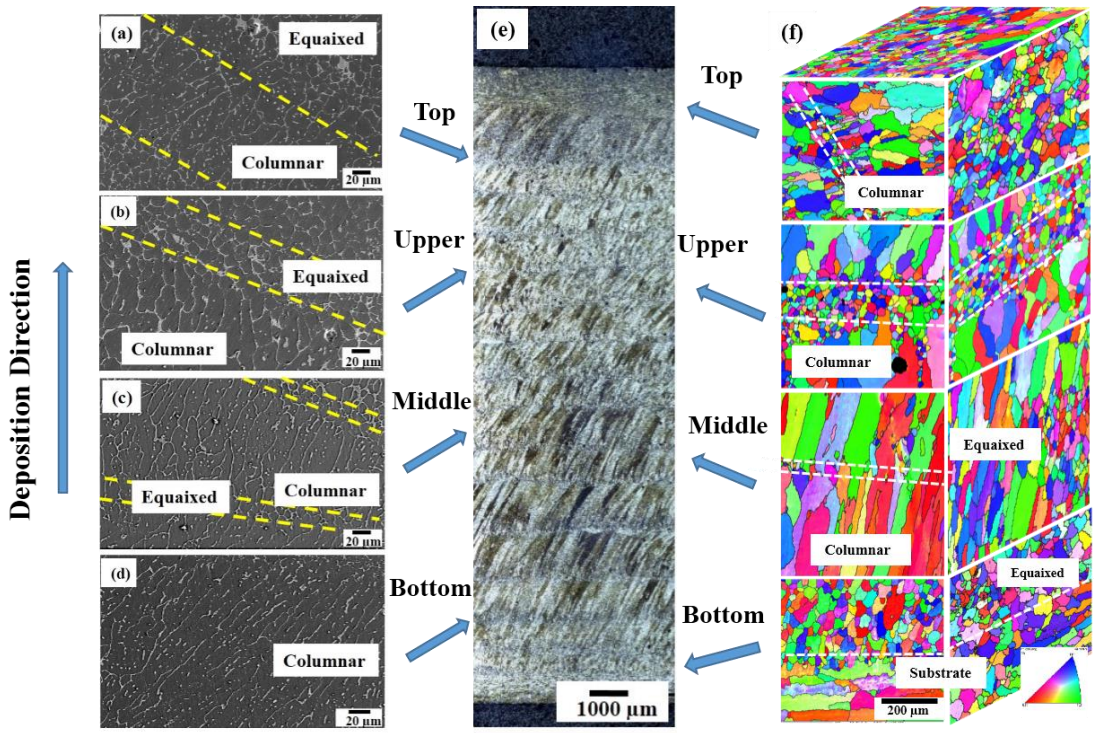

Figure 4 The microstructure maps of the WC deposit: the SEM photo at the (a) top zone; (b) upper zone; (c) middle zone; (d) bottom zone; (e) the cross section; (f) the 3D IPF photo.

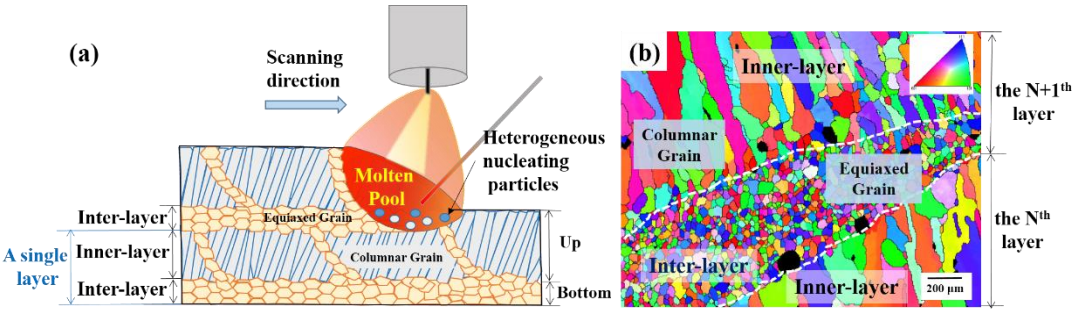

Figure 5 (a) The schematic diagram of the grain morphology evolution;

(b) the IPF of the equiaxed and columnar grains

In this work, the WC and AC deposits were obtained by adjusting the cooling mode of the substrate. Their macrostructural morphologies are depicted in Figure 6. It clearly shows the presence of multiple bumps on the side surface of the WC deposit, whereas the side surface of the AC deposit is relatively flat. The widths of WC and AC deposits are equal to 6.93±1.1 mm and 7.83 ± 0.9 mm, respectively.

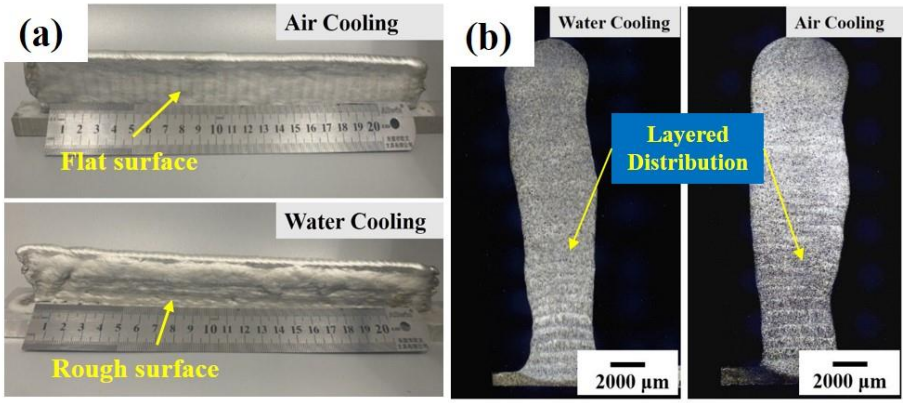

Figure 6 The macrostructural morphologies in the AC and WC deposits:

(a) the macro morphology; (b) the cross section.

Figure 7 shows the microstructural characteristics of the AC and WC deposits. According to Figures 7(a,d), both deposits exhibit alternating distributions of the equiaxed grains in the inter-layer zone and columnar grains in the inner-layer zone. Table 4 lists the quantitative statistics on the microstructural characteristics of the WC and AC deposits. The area fraction of the columnar grains in the AC deposit was 69%, while its value obtained for the WC deposit was 85%. Figures 7(b,e) show that both the AC and WC deposits contain typical columnar dendritic arrays and the eutectic θ phase (Al_2Cu) precipitated in the inter-dendrite region and at the grain boundaries.

The experimentally measured PDAS values of the WC and AC deposits are 21.9±6.7 and 34.6±8.9 μm, respectively. Compared with the WC deposit, the AC deposit exhibited larger PDAS and number of pores in the equiaxed grain zone. As shown in our previous study [40], the thermal cycling and accumulation in the WAAM process influence the supersaturation of Cu in the α-Al matrix, resulting in the precipitation of the θ' phase. Figures 7(c,f) indicate that the θ' phase precipitated near θ phase due to thermal accumulation. The volume fractions of the θ phase in the AC and WC deposits are equal to 7.3% and 5.8%, respectively. The volume fraction of the θ phase in AC deposit was slightly higher than that in the WC deposit. Owing to the high cooling rate of the WC deposit, a larger copper amount dissolved in the α-Al matrix during the solidification of the molten pool. Therefore, a lower amount of the θ phase (Al_2Cu) precipitated from the α-Al matrix in the WC deposit than in the AC deposit.

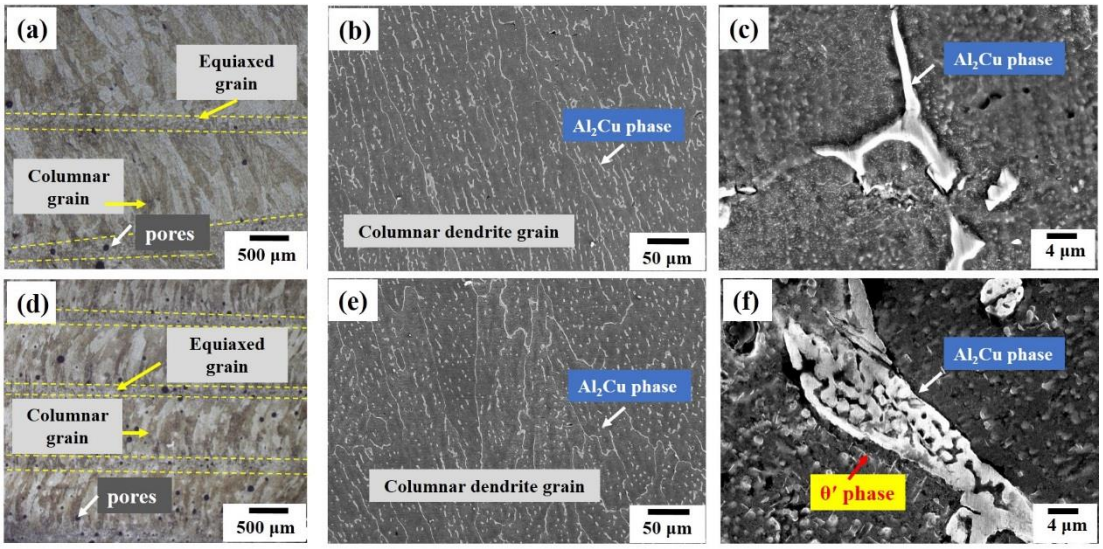

Figure 7 The microstructure in AC and WC deposits: (a) optical microscope for WC deposit; (b) SEM maps of WC deposit; (c) precipitates for WC deposit; (d) optical microscope for AC deposit; (e) SEM maps of AC deposit; (f) precipitates in the AC deposit.

Table 4 The quantitative statistics on microstructure characteristics in WC and AC deposits.

	AC deposit	WC deposit
The volume fraction of θ phase (%)	7.3±1.5	5.8±2.5
The proportion of columnar grain (%)	69.24±8.4	85.36±4.6
The width of columnar grains (μm)	112	109
The diameter of equiaxed grains (μm)	13.15	22.39
The primary dendrite spacing (μm)	34.6±8.9	21.9±6.7

3.2 Precipitate characteristics

Figures 8(a,b) show the HAADF-STEM images of the precipitates in the WC and AC deposits, respectively. The block θ phase and plate-like phase precipitate in the α-Al matrix are present in both deposits. The plate-like phase can be identified as the θ′ phase by selected electron area diffraction (SEAD) and high-resolution TEM (HRTEM) images see in Figures 8(c-f). According to the obtained HRTEM image, the orientational relationship between the α-Al matrix and θ phase is $(100)_{\theta'}$// $(100)_{\alpha\text{-Al}}$ and $[100]_{\theta'}$// $[100]_{\alpha\text{-Al}}$ (see Figures 8(e, f)). The semi-coherent interface between the θ phase and the α-Al matrix can be attributed to the solid-state transformation from the α-Al to the θ phase. As shown in the HADDF-STEM images (Figures 8(a,b)), the volume fraction of the θ′ phase in the WC deposit is apparently lower than that in the AC deposit. The dimensions of the θ′ phases in the AC and WC deposits are 470±124 nm × 12 nm (length × width) and 227±49 nm × 8 nm, respectively, because Cu atoms were trapped in the α-Al matrix during the solidification and cooling of the molten pool due to the large cooling rate of the WC deposit.

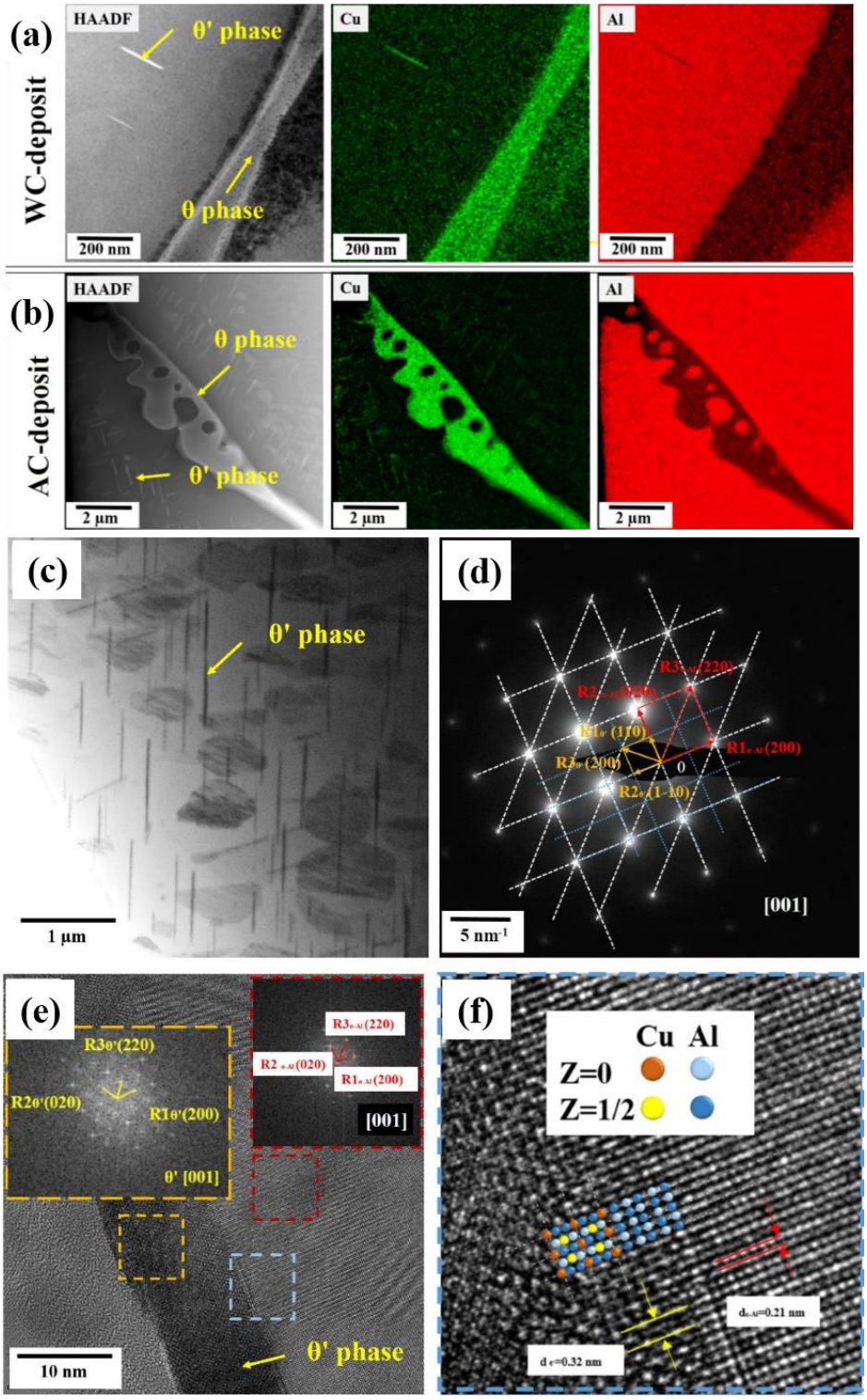

Figure 8 (a) HADDF-STEM image in WC deposit; (b) HADDF-STEM image in AC deposit; (c) the HRTEM image of θ′ phase in AC deposit; (d) the selected area electron diffraction (SAED) spot of θ′ phase; (e) the HRTEM of θ′ phase; (f) interfacial atomic arrangement of the θ′ phase.

Figure 9(a) shows a HAADF-STEM image of $Al_3(Zr,Ti)$ particles. These particles can be distinctly observed inside the equiaxed grains. The EDS maps demonstrated that these particles were enriched with Zr and Ti, which is consistent with the phase constituents identified by the SAED patterns and EDS results. Based on the SAED patterns and atomic resolution HAADF-STEM images, these Zr/Ti-enriched particles can be confirmed as $L1_2$-$Al_3(Zr,Ti)$ particles. Many researchers [41, 42] reported that heterogeneous nucleation of α-Al on the $L1_2$-$Al_3(Zr,Ti)$ particles promotes the formation of equiaxed grains during additive manufacturing.

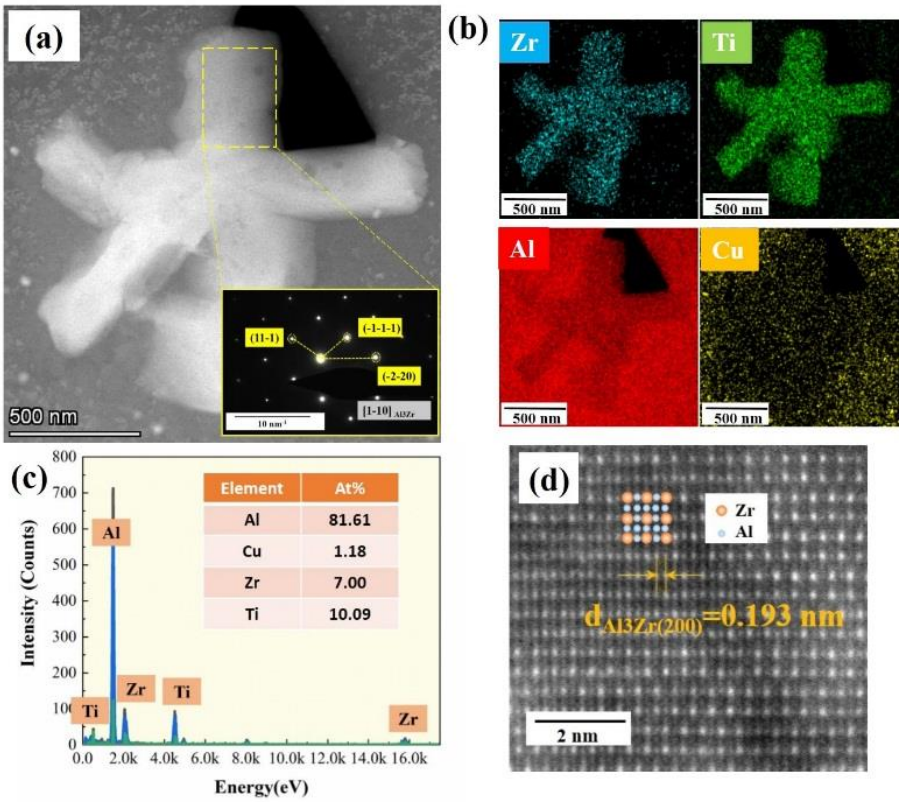

Figure 9 The TEM microstructure of $Al_3(Zr,Ti)$ phase: (a) the HADDF-STEM image and diffraction spot; (b,c) the EDS mapping results;(d) the atomic resolution HAADF-STEM image

3.3 Pore characteristics

Statistical analysis of the pores was performed by micro-CT to determine their size and shape. Figures 10(a,d) show the distribution of the pores in the WC and AC deposits, and the corresponding measurement results are listed in Table 5. The porosities of the

AC and WC deposit are 1.29% and 1.21%, respectively, while their median pore diameters are equal to 17 and 9 μm, respectively. The volume fraction of the pores in the WC deposit was smaller than that in the AC deposit.

Table 5 The quantitative statistical results of the micro-CT tests in the WC and AC deposits.

	Porosity (%)	Mean Diameter (μm)	Mean Volume (μm^3)	Mean Surface Area (μm^2)
WC-deposit	1.21	15.34	12759.8	1795.48
AC-deposit	1.29	20.38	13911.0	2214.22

Figures 10(b,e) show the D_e distributions of the pores along the deposition direction. At D_e<35 μm, the pore distribution shows no visible characteristics. However, at D_e >35 μm, it exhibits a distinct layered structure. These pores are mainly present in the equiaxed grain zone of the interlayer. The average spacings between the adjacent pore strips in the AC and WC deposits are 1561 and 1175 μm, respectively. Figures 10(c,f) show the pore number distributions (D_e>35 μm) along the deposition direction, which exhibit period-fluctuating characteristics at certain intervals. The spacing between the adjacent peaks of the WC deposit was smaller than that observed for the AC deposit. For both the WC and AC deposits, the peaks of the pore number and size distributions overlap considerably.

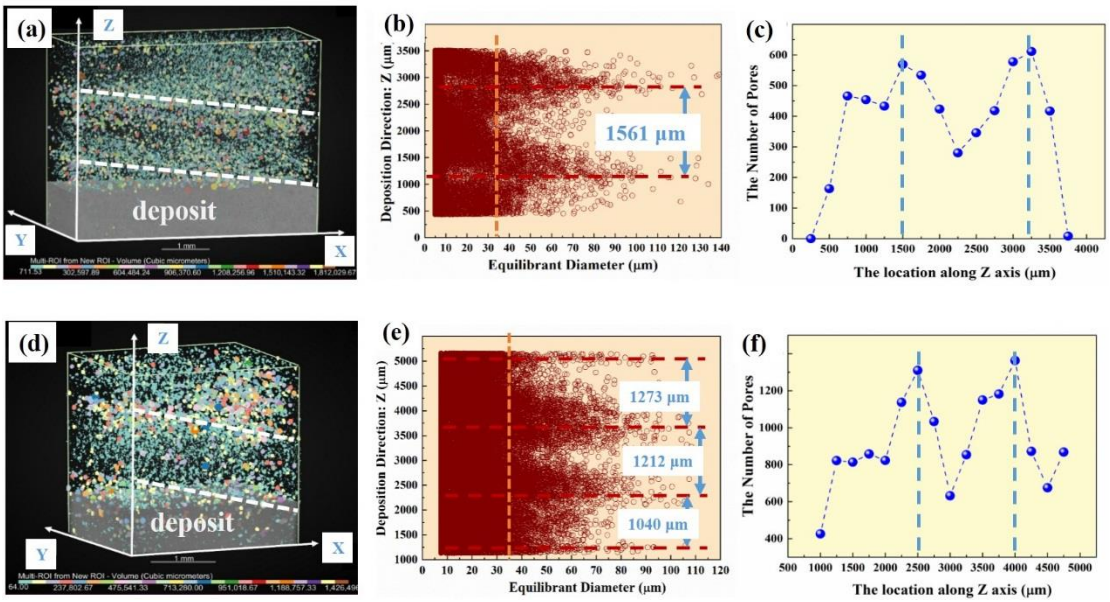

Figure 10 (a,d) The 3D distribution of pore morphology in micro-CT test of the AC and WC deposits; (b,e) the relationship of D_e with the location along Z axis in AC and WC deposits; (c,f) the relationship between the number of the pores with the location along Z axis in AC and WC deposits

Figure 11(a) shows the relationship between D_e and the sphericity of pores calculated according to the following equation:

$$Sphericity = \frac{4\pi\left(\frac{3V_P}{4\pi}\right)^{\frac{2}{3}}}{S_P} \quad (6)$$

where V_P is the pore volume, and S_p is the surface area of the pores. The average sphericities of pores in the WC and AC deposits are equal to 0.91±0.07 and 0.89±0.08, respectively. Although the deposition conditions of the WC and AC deposits are different, their sphericity values are relatively high. When the D_e of pores is small, their sphericity is close to 1. Figure 11(b) shows the relationship between the surface area and the D_e of each pore. The D_e of pores in the WC deposit was smaller than the magnitude obtained for the AC deposit, and their average values were 15.34 and 20.38 μm, respectively.

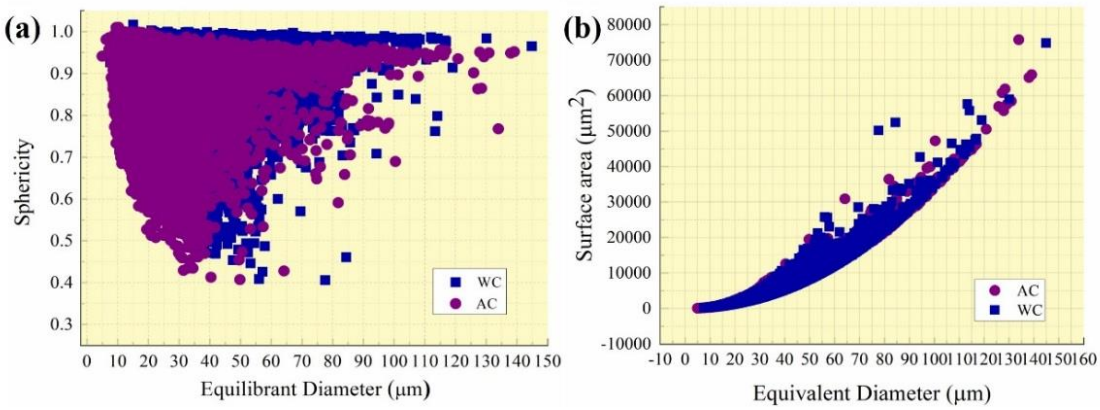

Figure 11 (a) The relationship between the sphericity with D_e of the pores in the WC and AC deposits; (b) the relationship between the surface area with D_e of the pores in the WC and AC deposits

3.4 Mechanical performance

3.4.1 Micro-hardness

Figure 12(a) shows the two-dimensional distribution of the microhardness data obtained in the WC deposit. The indentations and their distributions are presented in Figures 10(b,c), respectively. A higher hardness of 86±4 HV was obtained for the equiaxed grain zone, and a lower hardness of 76±7 HV was measured for the columnar grain zone. Owing to the alternating distribution of the equiaxed and columnar grains, the microhardness also shows an alternating distribution of the high and low zones. The average hardness values of the WC deposit (corresponding to an equiaxed grain volume fraction of 31%) and AC deposit (corresponding to an equiaxed grain volume fraction of 15%) were 73±3 and 81±5 HV, respectively.

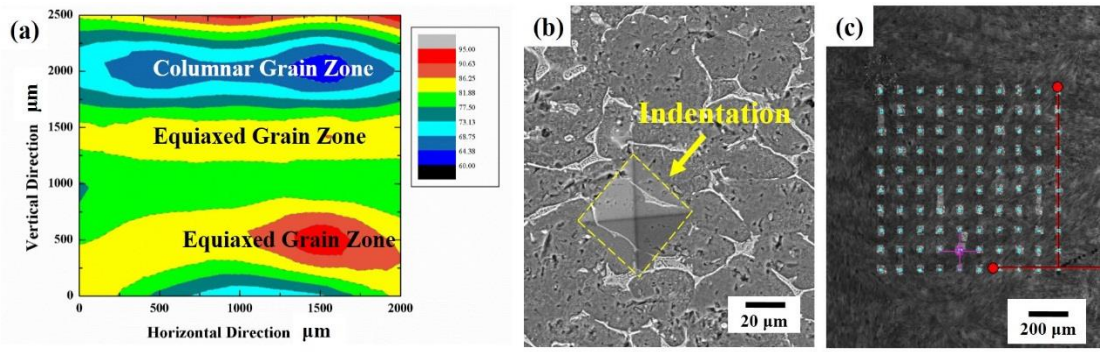

Figure 12 (a) The 2D distribution of micro hardness test results of WC deposit; (b) the indentation for the micro hardness test; (c) indentation location map for the 2D results.

3.4.2 Tensile properties

Figure 13 shows the stress-strain curves obtained during the tensile testing of the AC and WC deposits. Figures 13(a,b) indicate that the ultimate strength (UTS), yield strength (YS) and elongation (EL) of the WC deposit are equal to 247.7±17.7 MPa, 110.1±6.3 MPa and 11.9±0.7%, which are higher than those of the AC-deposit by 10.76%, 15.78%, and 26.78%, respectively. According to the Portevin-Le Chatelier (PLC) effect, plastic instability leads to deformation localization and produces the stress-strain curve with sawtooth pattern [43]. The obtained tensile curve contains a jagged wave at the plastic deformation stage (Figure 13(a)), suggesting an apparent PLC effect during the tensile deformation of the WAAM-processed 2219 Al alloy. Figure 14 shows the fracture morphologies of the WC and AC deposits after the tensile testing, which exhibit pores and small dimples. The pore sizes of the AC deposit were larger than those of the WC deposit. Moreover, cracks were formed along the grain boundaries and small dimples were detected in the fracture morphologies of the WC and AC deposits, indicating that the observed fractures had typical characteristics of ductile fractures. Figure 13(c) shows the work hardening rate-true strain curves, demonstrating the work hardening rate gradually decreases with strain. Additionally, the curves obtained for the WC and AC deposits exhibit similar trends and can be divided into three stages: a rapid decline stage (I), a slow decline stage (II) and a stable stage (III), corresponding to the elastic deformation stage, the yield stage, and the plastic deformation stage of the true stress-strain curve, respectively. The observed change in the work hardening rate was caused by the multiplication rate of dislocations during the tensile tests. The work hardening exponent (n) value characterizes the ability of a material to uniformly deform. The higher is the value of n, the larger is the damage resistance of the alloy. According to the true stress-strain curve depicted in Figure 11(c), the n values of the WC deposit and AC deposit during plastic deformation are equal to 0.32 and 0.3, respectively, which indicates that the plasticity of the WC deposit is similar to that of AC deposit.

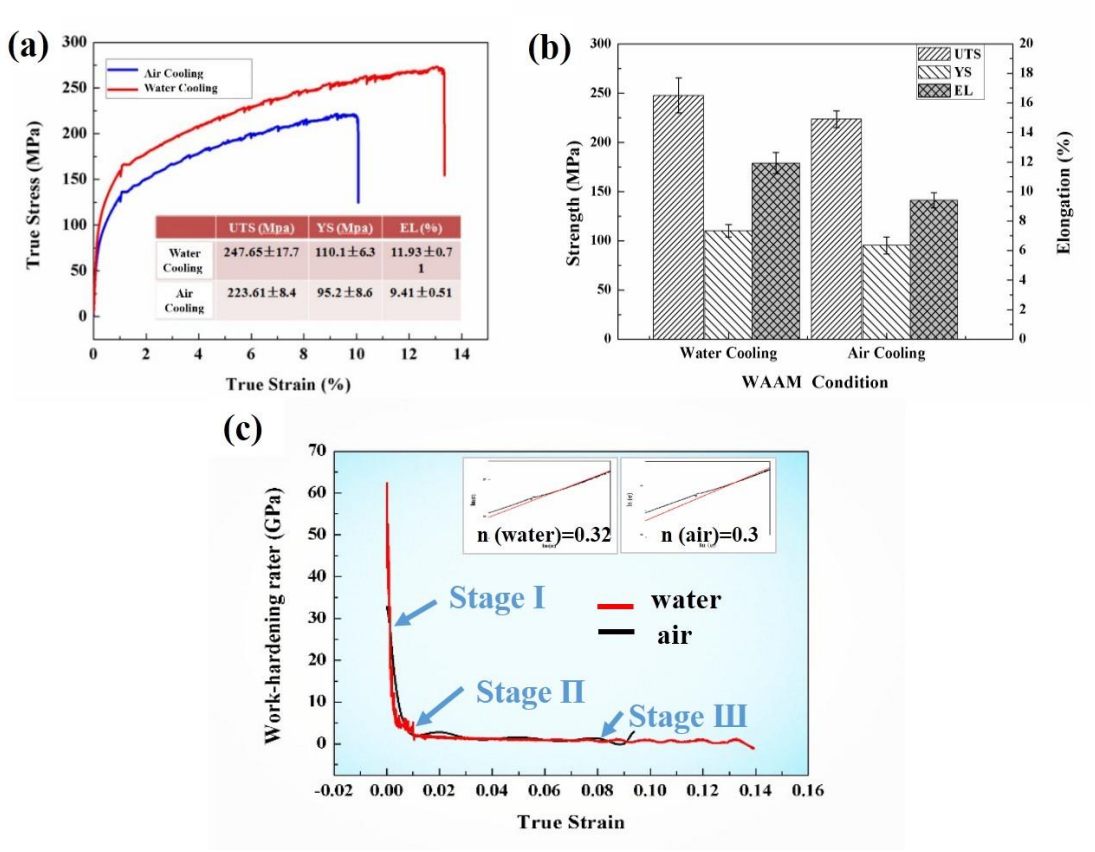

Figure 13 (a) The true stress-strain curves of the WC and AC deposits; (b) the tensile tests results; (c) the work hardening rate-true strain curves and work-hardening exponent (n) of WC and AC deposits.

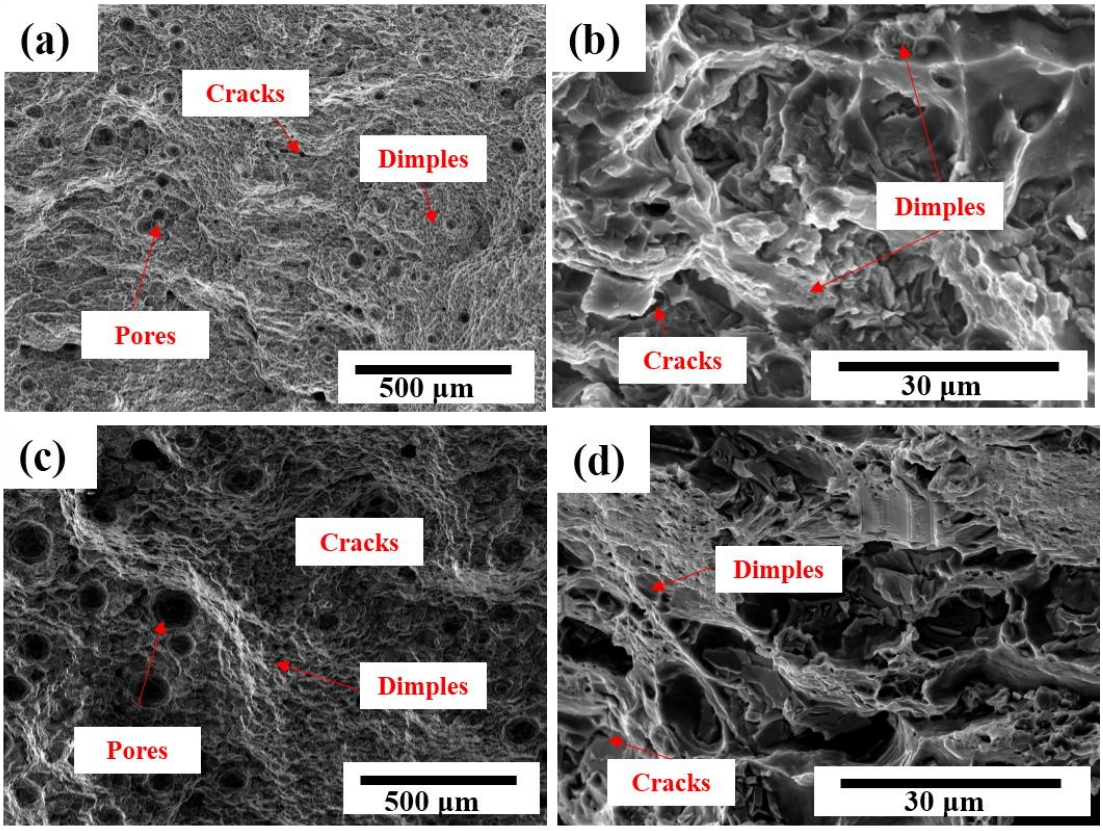

Figure 14 The fracture morphology of the WAAM-processed 2219 Al alloy:

(a,b) WC deposit; (c,d) AC deposit.

4. Discussions

4.1 Primary dendrite arm spacing

According to the SEM images depicted in Figures 7(b,e), an apparent dendrite refining phenomenon is observed in the WC deposit. The PDAS during the alloy dendrite growth can be expressed as follow [44]:

$$\lambda = 2.83\left(k\Delta T_0 D\Gamma\right)^{\frac{1}{4}} R^{-\frac{1}{4}} G^{-\frac{1}{2}} \quad (7)$$

Where $\Delta T_0=T_L-T_e$, T_L is the liquids temperature, and T_e is the eutectic temperature. ΔT_0 is the equilibrium solidification range, which was calculated using the JmatPro software. D is the diffusion coefficient of the Al solute in liquid, and Γ is the Gibbs-Thomson coefficient. R is solidification rate. G is the temperature gradient. Table 6 lists the parameters required in Equation (7). Figure 15(a) shows the simulated data of G, R, and

ε in the molten pool at the 6th layer. Based on the G and R value of L_3 position (approximately 200 μm from the bottom of the molten pool) in the simulated temperature field of molten pool as shown in Figure 15(b), the PDAS at L_3 position in the WC and AC samples is calculated. Table 7 lists the data of G and R. The λ_c values determined for the 6th layers of the WC and AC deposits are equal to 18.11 and 25.36 μm, respectively.

In order to compare the calculated and experimentally measured PDAS results of the WC and AC samples. The triangle method was used to measure the PDAS approximately 200 μm from the bottom of the molten pool at the 6th layer in the WC and AC samples. The λ_{exp} values of the WC and AC deposits are 22.9±3.7 and 30.4±2.3 μm, respectively. Thus, the calculated PDAS values are in good agreement with the experimental values. Notably, the PDAS of the WC deposit is smaller than that of the AC deposit because of the larger cooling rate (ε) and temperature gradient (G) of the former system (the larger is the cooling rate, the finer are the dendrites).

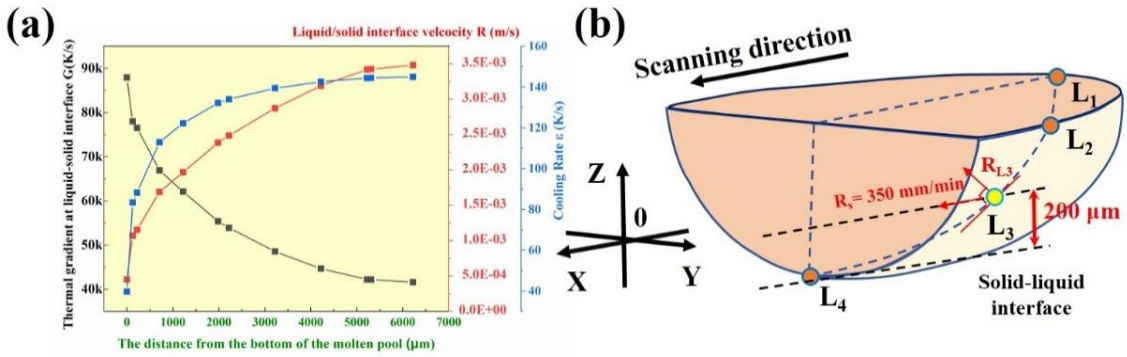

Figure 15 (a) The simulation results of temperature gradient (G), solidification velocity (R), and cooling rate (ε) variation trend in a molten pool ;(d) the schematic diagram of the location for calculated and measured PDAS in a molten pool (L_3).

Table 6 The physical property parameters calculated in Equation (7).

Physical Property	Value (units)
Liquidus temperature (T_L)	915.41 (K)
Eutectic temperature (T_e)	821.16 (K)
Equilibrium solidification range (ΔT_0)	94.25 (K)
Liquidus slope (m)	-2.6
Partition coefficient (k)	0.14
Diffusion coefficient in liquid (D)	3.0×10^{-9} (m^2/s)
Gibbs Thomson coefficient (Γ)	1.1×10^{-6} (Km)

Table 7 The calculated and measured results of the primary dendrite arm space in AC and WC samples

	R (m/s)	G (K/m)	λ_c (μm)	λ_{exp} (μm)
WC deposit	0.00164	125527.1	18.11	22.9±3.7
AC deposit	0.00115	76487.4	25.36	30.4±2.3

4.2 Formation of heterogeneous microstructure

Based on Hunt's model [45], Gäumann et al. established critical conditions for the transition between the columnar grains and equiaxed grains (CET). The obtained relationship can be expressed as [46]:

$$G = \frac{1}{n+1}\sqrt[3]{\frac{-4\pi}{3\ln(1-\varphi)}}N_0^{\frac{1}{3}}\left(1-\frac{\Delta T_n^{n+1}}{(\alpha R)^{\frac{n+1}{n}}}\right)(\alpha R)^{\frac{1}{n}} \quad (8)$$

Where N_0 is the density of nucleation sites, ΔT_n is the nucleation undercooling temperature, φ is the volume fraction of equiaxed grains, G is the temperature gradient, and R is the solidification rate. α and n are constants related to the utilized materials itself. Hunt [45] suggested that the alloy microstructures consisted of columnar grains at $\varphi < 0.66\%$ and fully equiaxed grains at $\varphi > 49\%$. According to the calculation results, $n = 2.7065$, $\alpha = 5.61504 \times 10^6$, and $N_0 = 10^{12}/m^3$ [47].

Figure 16 shows the CET maps corresponding to the simulated solidification conditions for the 1st, 6th, 15th and 30th layers of the AC and WC deposits expressed by the blue and grey frames, respectively. The arrow direction indicates the solidification conditions from the boundary to the center of the molten pool. According to the simulated temperature field of the molten pool (Figure 17), the solidification conditions of the first layer of the molten pool in WC deposit (ε = 35-427 K/s, G = 199705-130000 K/m) and AC deposit (ε = 22-264 K/s, G = 166000-76000 K/m) were obtained. The microstructures of the first layers of the molten pools in the WC and AC deposits should contain fully columnar grains. However, according to the experiment data presented in Figure 18, the microstructure of the molten pool boundaries in the AC deposit consisted of equiaxed grains, which were transformed into columnar α-Al grains deflected along the direction of the temperature gradient. Though the formation conditions of the

equiaxed and columnar grains have a certain relationship with the value of G/R, the nucleation site number N_0 also plays a remarkable on the formation of grain morphology. Although there is a large G/R value at the molten pool boundaries, the high value of N_0 leads to the formation of equiaxed grains instead of columnar grains.

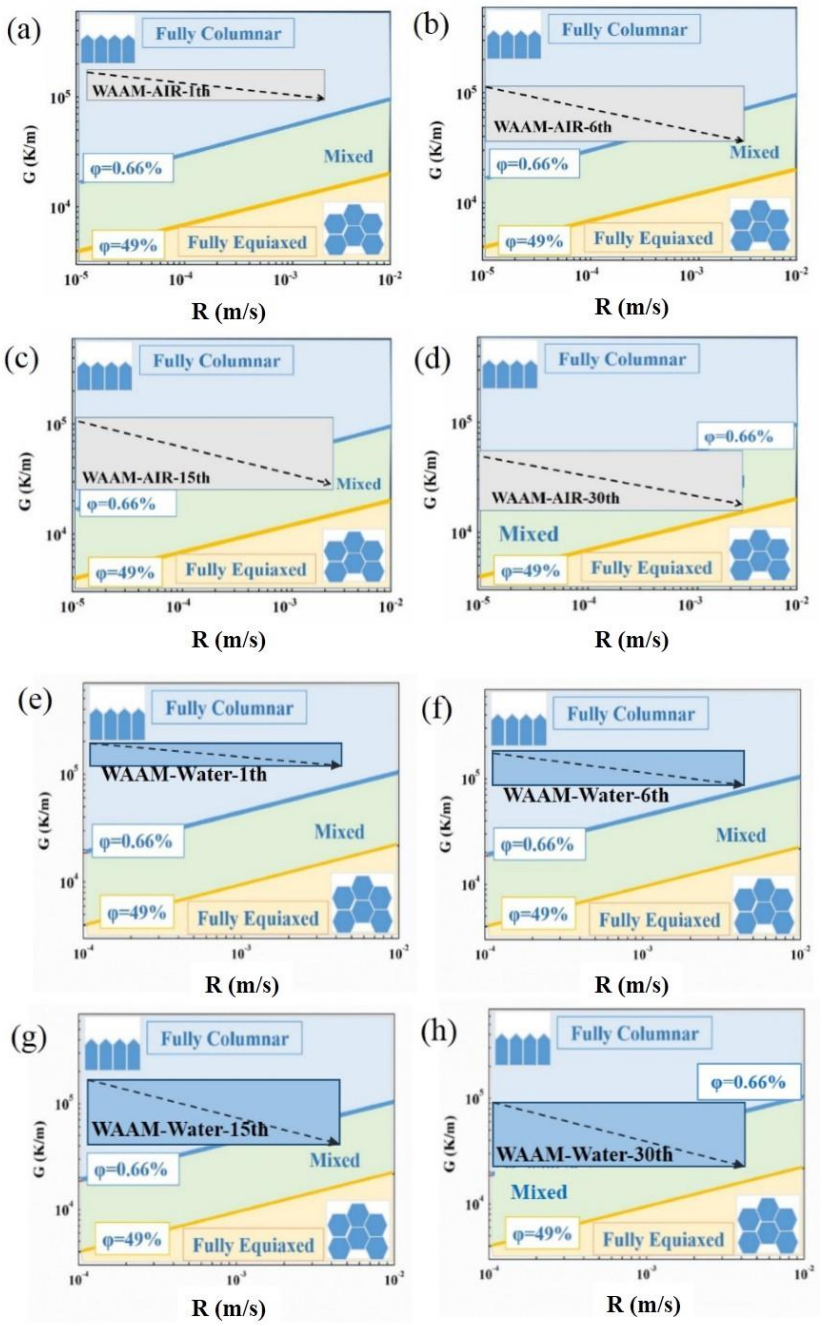

Figure 16 The calculated CET maps of the WAAM-processed 2219 Al alloy in AC and WC deposits: (a,e) the 1st layer; (b,f) the 6th layer; (c,g) the 15th layer; (d,h) the 30th layer.

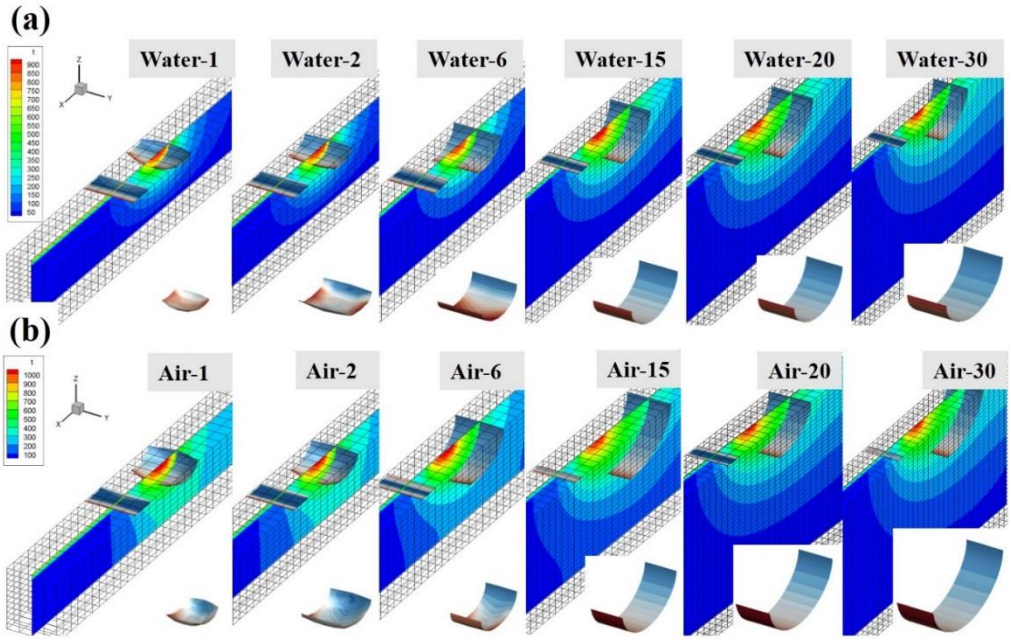

Figure 17 The simulated temperature field of the molten pool in the1st, 2nd, 6th, 15th, 20th, 30th layer:(a) WC deposit; (b) AC deposit.

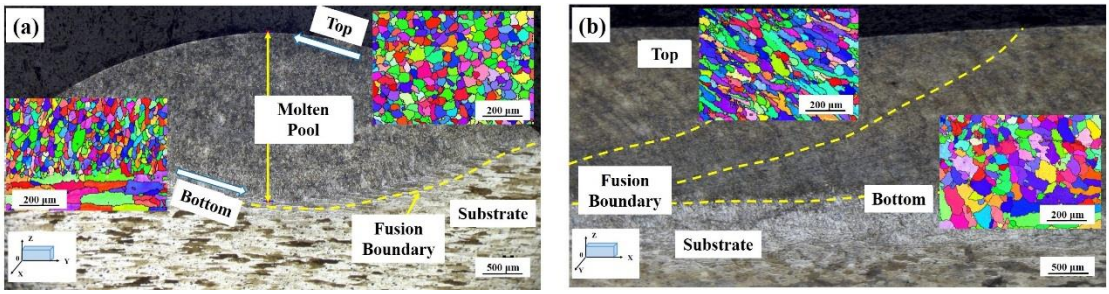

Figure 18 The microstructure of the 1st layer in WAAM-processed AC deposit: (a) yoz plane; (b) xoz plane.

According to the results of previous studies conducted by A.E. Ares[48], McCartney[49], and Martorano [50] , when the value of N_0 increased, the volume fraction of equiaxed grains in CET maps increased significantly. Figure 19 shows the CET maps of the WAAM-processed 2219 Al alloy with different N_0 values (here, the red rectangular frame denotes the range of the simulated temperature gradient and solidification rate in the first layer of the molten pool). When N_0 is lower than $10^{13}/m^3$, the solidification microstructure still shows columnar grains in the CET maps. Meanwhile, when N_0 is larger than $10^{14}/m^3$, the microstructure contains a mixture of equiaxed and columnar grains, that equiaxed grains are likely be formed when N_0

increases to $10^{14}/m^3$.

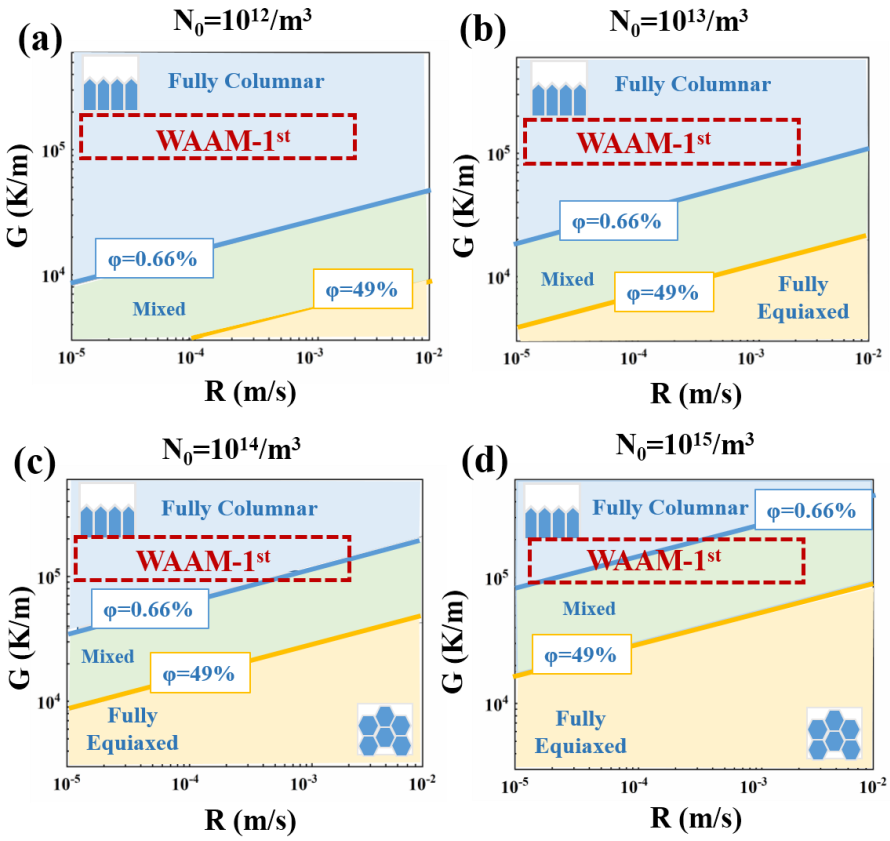

Figure 19 The CET maps of the WAAM-processed 2219 deposits under different N_0:

(a) N_0 =$10^{12}/m^3$; (b) N_0 =$10^{13}/m^3$; (c) N_0 =$10^{14}/m^3$; (d) N_0 =$10^{15}/m^3$.

Because the substrate is the 2024 Al alloy, it does not contain alloying elements such as Zr and Ti that can promote the formation of heterogeneous nucleation particles. Therefore, heterogeneous nucleation particles likely originate from the solidification process rather than from the 2024 Al substrate. Some alloying elements in the ER2319 wire, such as Zr, Ti and V, can form heterogeneous nucleated particles, including Al_3Zr and Al_3Ti ones. To verify this hypothesis, the Thermo-Calc software was used to calculate the equilibrium phase diagram of Al-6.9Cu-0.3Mn-0.2Zr-0.14Ti (wt.%) (Figure 20(a): the dotted line denotes the composition of the WAAM-processed 2219 Al alloy). According to the phase diagram, when the temperature decreases to the liquids temperature (1035 K), Al_3Zr particles are first generated at the early solidification stage. When the temperature further decreases to 917.5 K, Al_3Zr particles continue to precipitate. The solidification precipitation sequence of the Al-6.9Cu-0.3Mn-0.2Zr-0.14Ti (wt.%) alloy during Scheil solidification was calculated by

Thermo-Calc software, as shown in Figure 20(b). It was found that Al_3Zr particles first precipitated from the liquid at 1035 K during the solidification process followed by the peritectic reaction $L + Al_3Zr \rightarrow \alpha$-Al at 917.5 K. The solidification interval of Al_3Zr particles is 117.5 K. Thus, Al_3Zr particles likely precipitate from the alloying melt before the nucleation of α-Al particles that are subsequently formed through peritectic reaction. Hence, Al_3Zr particles can be used as heterogeneous nucleation particles to increase the N_0 value and promote the formation of equiaxed α-Al grains.

The obtained results indicate the existence of the optimal conditions for the formation of equiaxed grains during the solidification of the WAAM-processed 2219 Al alloy. In fact, the possible reason for the equiaxed grains transform to columnar grains from the boundaries to the center of the molten pool is that the precipitation of Al_3Zr particles are inhibited with the increase of cooling rate. Many researchers [19, 51] reported that the cooling rate strongly effects the precipitation of Al_3Zr particles. Mathieu Opprecht et al. [41] confirmed the variation in density of heterogeneous nucleating particles according to molten pool depth and decrease gradually with the increase of cooling rate. When moving towards the center of the molten pool, the increase of cooling rate has a strong effect on the transient nucleation mode. As a result, the nucleation of Al_3Zr particles were prevented. Thus, when the solid/liquid interface without Al_3Zr particles the columnar grain growth occurs. The relationship between precipitation rate of Al_3Zr particles and cooling rate is known from the literatures [19, 41, 51]. Thus, the equiaxed grain regions exist at the melt pool boundary of the WAAM-processed 2219 Al alloy. Figure 21 displays the simulated mushy zone (917.5–1035 K) of Al_3Zr particles in the molten pool of the 1^{st}, 6^{th}, 15^{th}, and 30^{th} layers in the AC and WC deposits. It shows that the width of the mushy zone of Al_3Zr particles gradually increases with an increase in the number of deposition layers. Moreover, the mushy zone width of the AC deposit is larger than that of the WC deposit. The wider mushy zone of Al_3Zr particles indicates their relatively large number, which promotes the formation of equiaxed grains. This conclusion is consistent with the obtained experimental data.

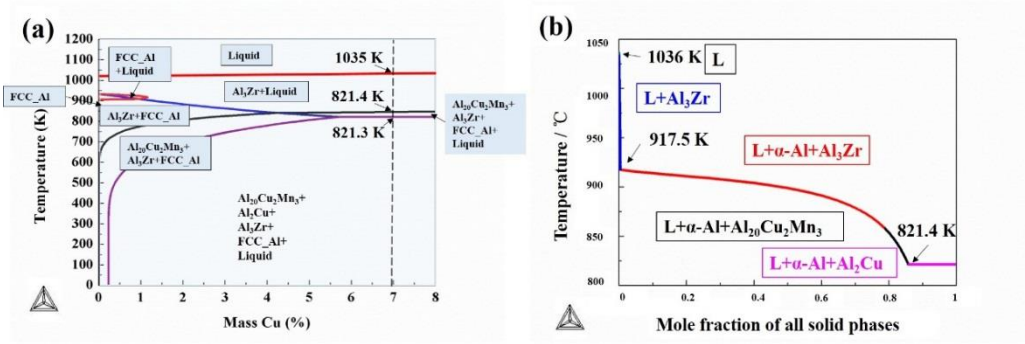

Figure 20 (a) Equilibrium phase diagram and (b) the Scheil solidification sequence of the Al-xCu-0.3Mn-0.2Zr-0.14Ti (wt.%) calculated by Thermo-Calc software.

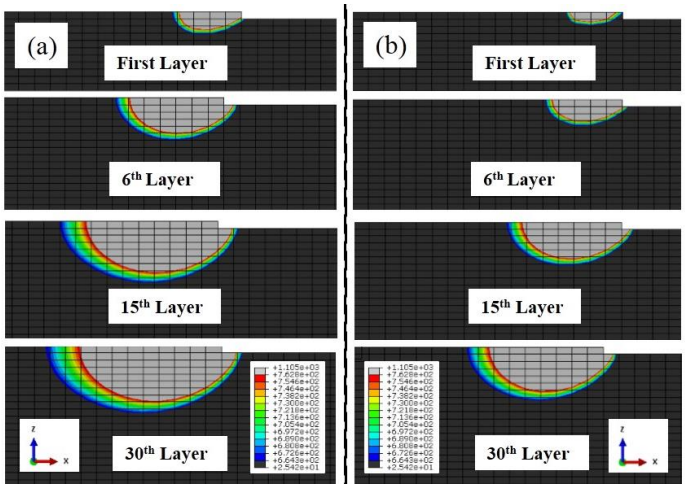

Figure 21 Simulated temperature field diagram of solidification interval of Al_3Zr particles in different deposition layers in the WAAM-processed 2219 Al alloy:

(a) AC deposit; (b) WC deposit.

4.3 Pores defect

The formation of pores during the solidification of the molten pool generally consists of three stages: nucleation, growth and floating. The nucleation stage requires the presence of a supersaturated gas in the liquid metal and sufficient energy to form a pore core. The equation describing the pore nucleation process can be written as follows:

$$E_P = -(p_h - p_L)V_p + \sigma A[1 - \frac{A_a}{A}(1 - \cos\theta)] \quad (9)$$

Where E_P is the energy required to form a pore core, p_h is the gas pressure inside the pore, p_L is the pressure of the liquid, V_p is the volume of the pore core, σ is the stress generated between phases, A is the surface area of the pore core, A_a is the area of the

adsorption force, and θ is the wetting angle between the pore core and the existing surface. According to Equation (8), when pores are formed on the existing surface, the nucleation energy E_p can be reduced due to the lower interphase tension σ and higher A_a/A ratio. In addition, the area with the highest of A_a/A ratio has the largest pore generation probability. Therefore, the interfaces between dendrites are prone to pore nucleation. After the nucleation of pores, they continue to grow and may escape outward. The upward velocity of pores growth was calculated via the following equation:

$$v = \frac{2(\rho_1 - \rho_2)gr^2}{9\mu} \tag{10}$$

Where v is the pore floating speed, ρ_1 is the density of the liquid, ρ_2 is the density of the gas, g is the gravitational constant, r is the pore radius, and μ is the viscosity of the liquid. The larger the value of r, the greater is the value of ρ_1 and the smaller is the μ magnitude, which inhibits pore formation. However, when v is less than the solidification rate, pores are easily formed.

The possible reasons for the smaller number of pores in the WC deposit can be formulated as follows. (1) During the WC deposit formation, the heat conduction is fast, the heat accumulation is slow, and the cooling rate is high. When the cooling rate increases, the critical hydrogen content required for the formation of pores also increases [52]. Thus, the number and size of pores gradually decrease with an increase in the cooling rate. (2) Increasing the cooling rate promotes grain refinement. The increase in the grain boundary area limits the nucleation and growth of hydrogen pores. Therefore, the size and number of pores in the WC deposit are reduced. (3) The possibility of pore escape during the WAAM process depends on the relationship between the upward velocity of pore growth, solidification velocity, and escape distance. According to Equation (9), the larger is the pore diameter, the higher is the floating speed of the pores in the liquid metal and the greater is their possibility of escape. When the pore floating speed is less than the solidification velocity, the pores remain in the weld. Because the average diameter of the pores in AC deposits is 50.25 μm, their calculated floating speed is 0.47 mm/s, which is much lower than the solidification rate,

as a result, the pores cannot escape. Figure 22 shows the temperature fields of the molten pools of the WC and AC deposits obtained for the 1st, 6th, 15th, and 30th layers by finite element simulations. Because the penetration depth and layer height of the WC deposit are smaller than those in the AC deposit, the distance required to escape through the WC deposit is less than that obtained for the AC deposit, and the possibility of pores escape in the WC deposit is relatively high.

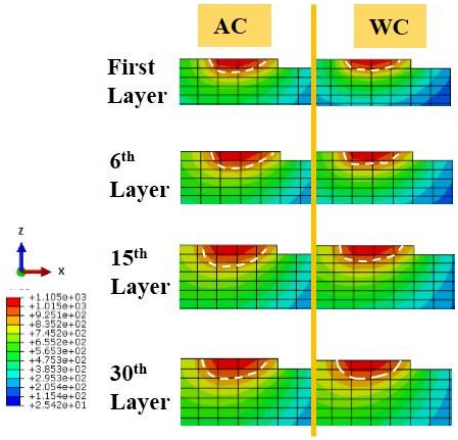

Figure 22 Simulation results of temperature field in molten pool of the WAAM-processed 2219 Al alloy.

4.4 Deformation of the heterogeneous microstructure

Figure 23 illustrates the *in-situ* DIC strain fields of the WC and AC deposits generated during the tensile process. The stratified deformation bands represent the land-like instability zones caused by the PLC effect [53, 54], which is mainly affected by dynamic strain aging [53]. Figure 23(a) shows the strain field of the AC deposit during the tensile process. With the continuous increase in strain, the strain field changes in the sequence "horizontal PLC band → concentration → fracture". At the start of the deformation, five horizontal PLC bands are distributed across the sample, after which the local strain becomes gradually concentrated at two positions. Finally, the sample breaks at the positions with the maximum strain. Figure 23(b) shows the strain field distribution of the WC sample obtained during the tensile process. With the continuous increase in strain, the strain field changes in the sequence "horizontal PLC bands →concentration → PLC bands → concentration → fracture", which is consistent with the repeated occurrence of local plastic instability caused by the PLC

effect. At the start of the tensile deformation, the local strain tends to focus on the four PLC bands in the sample and then gradually concentrates at one location. Afterwards, it is quickly distributed across the four bands and becomes concentrated at one location once again until the sample is broken. Compared with the AC deposit, the strain distribution in the WC deposit is more uniform and coordinated during deformation.

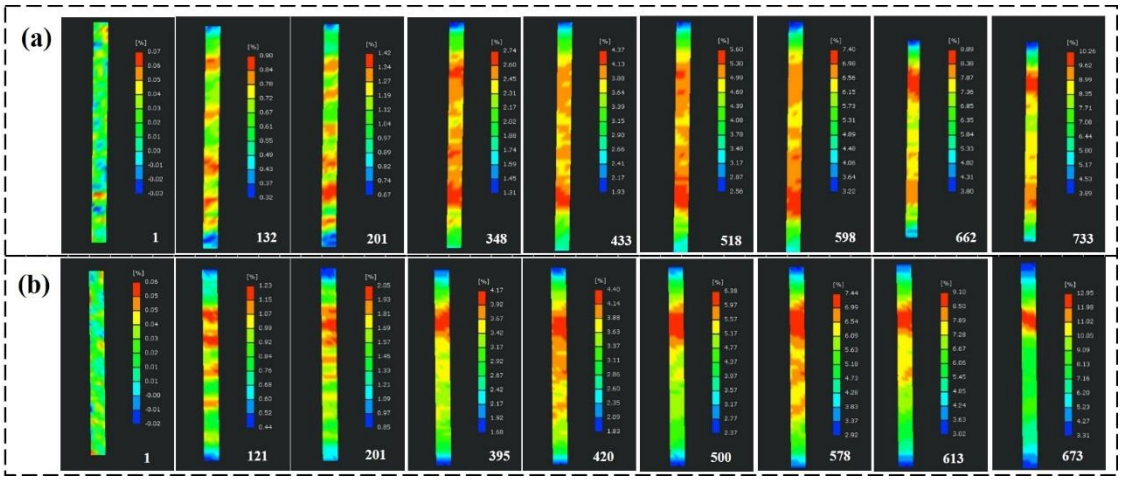

Figure 23 The digital image correlation strain field on the WAAM-processed 2219 Al alloy in the tensile tests: (a) the AC deposit; (b) the WC deposit.

Figure 24 shows the relationship between the maximum local strains in the WC and AC deposits obtained at various positions and times. The broken line represents the strain distribution along the line connecting points P1 and P2. The WC deposit exhibits the concentration and dispersed strain during deformation process, and its coordinated deformation ability is stronger than that of the AC deposit.

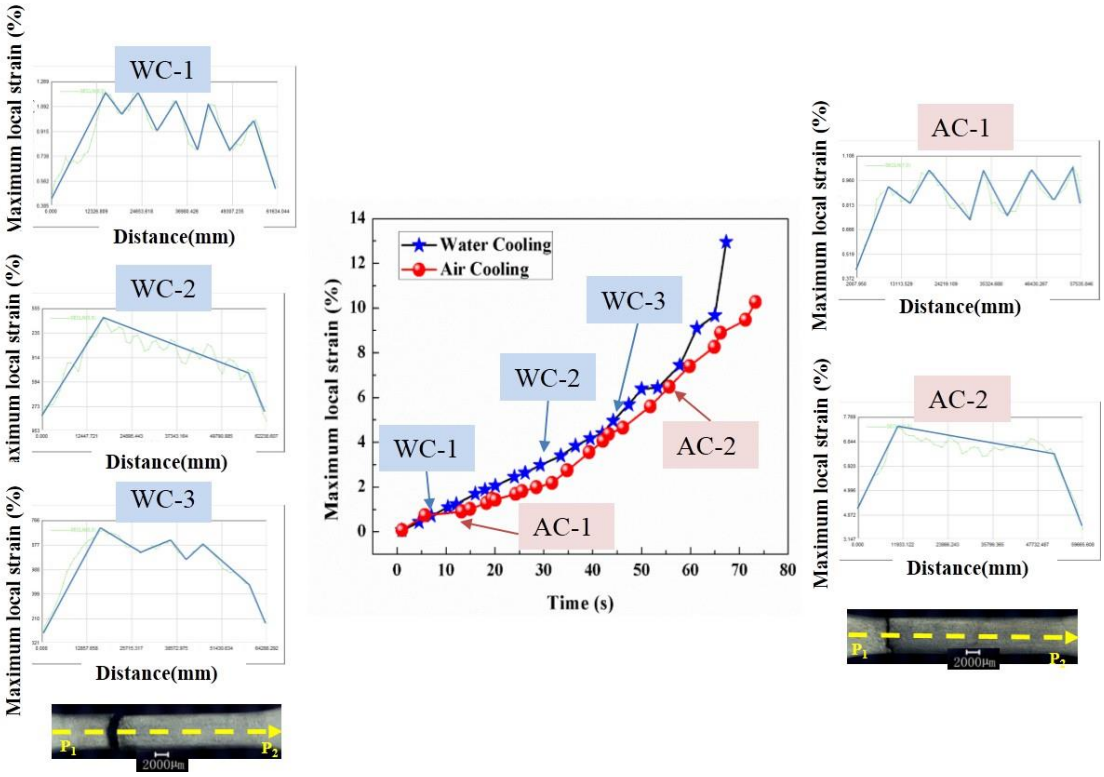

Figure 24 The relationship between the maximum local strain and time (the longitudinal strain at positions extracted from P_1 to P_2).

Figure 25 and 26 show the *in-situ* tensile curve and microstructural evolution in the WC deposit observed at various loading forces. As the loading force increases, both the columnar and equiaxed grains elongate in the horizontal direction. The horizontal average EL values of the columnar and equiaxed grains are equal to 8.1% and 2.7%, respectively. The obtained results indicate that the columnar grains undergo larger deformation and are more likely to be deformed than the equiaxed grains. At EL = 3%, cracks appeared around the columnar grain boundaries and pore defects. At EL = 7%, cracks were formed along the equiaxed grain boundaries in the equiaxed grain zone. The cracks at columnar grain boundaries were larger, longer, and wider than those at the equiaxed grain boundaries. Moreover, cracks were also formed in the eutectic θ phase. According to Figure 25, the saw tooth rheology and PLC effect are clearly reflected by the obtained stress-strain curve.

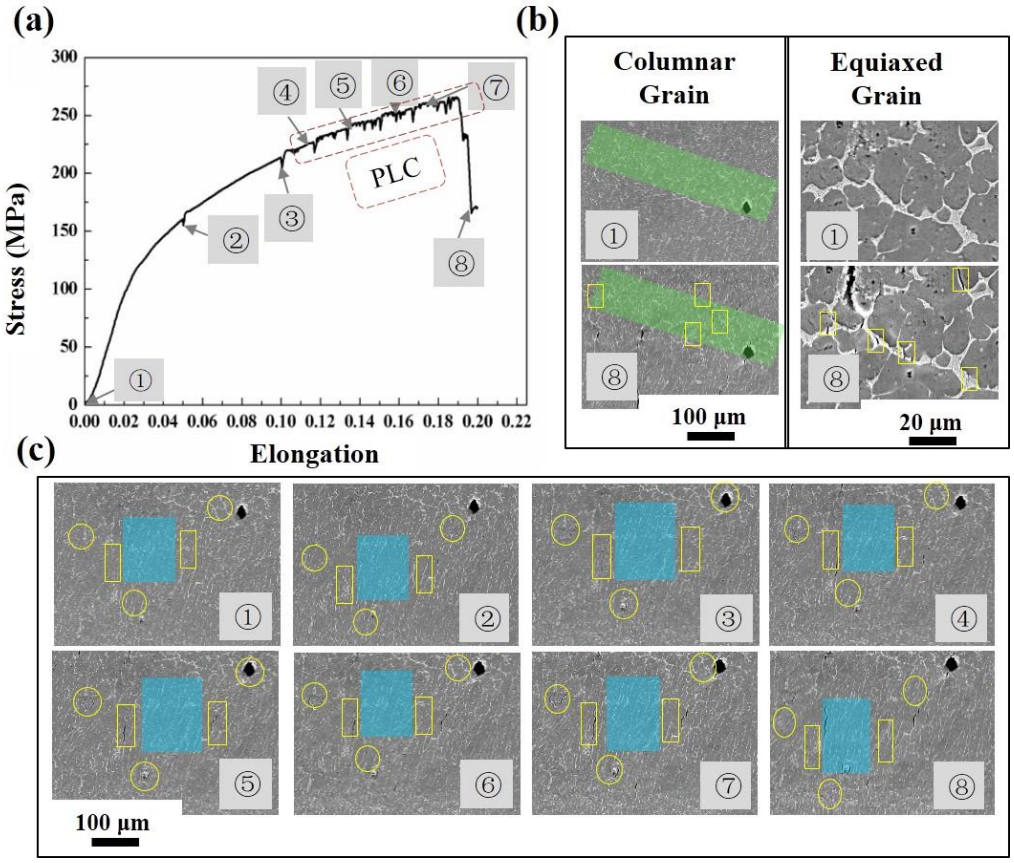

Figure 25 (a) The *in-situ* tensile testing curve; (b) the microstructure evolution at columnar zone and equiaxed zone; (c) cracks during tensile testing.

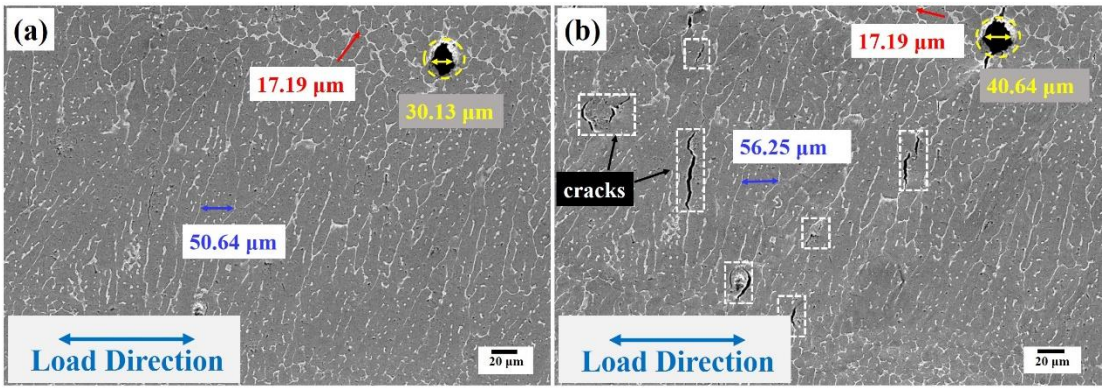

Figure 26 (a) The microstructure before *in-situ* tensile test; (b) the microstructure at fracture.

Figure 27 shows the geometrically necessary dislocation (GND) maps of the AC and WC deposits obtained during the *ex-situ* tensile deformation. Generally, the GND parameter reflects the uniformity of plastic deformation. A high GND value (the green

color in the GND maps) indicates large plastic deformation and high defect density. Using the strain gradient model proposed by Gao et al. [55], Kubin et al. [56] suggested that GND maps could be obtained from EBSD data and characterized stress distribution during the deformation process. Figures 27(ⅰ) and (ⅱ) show the IPF and GND maps of the WC and AC deposits obtained at different strains during tensile testing along the horizontal direction.

Figure 27(x-1), (x-2), and (x-3) show the IPF and GND maps obtained at strains of 0% and 5% and fracture during tensile tests. The IPF maps contain the apparent heterogeneous band structures composed of equiaxed and columnar grains. The volume fraction of the columnar grains in the WC deposit was higher than that in the AC deposit. As the tensile deformation increased, the width of the columnar and equiaxed grains increased as well. At EL = 5% (Figures 27(ⅰ-b-2) and (ⅱ-b-2)), the GNDs are mainly concentrated in the columnar grain zones of the WC and AC deposits. This indicates that the GND value in the columnar grain zone is larger than that in the equiaxed grain zone, and that the deformation in the columnar grain zone proceeds more intensely. Additionally, the columnar grain zones undergo plastic deformation before the equiaxed grain zones, which reflects the inhomogeneity and asynchrony between these two zone types. The GNDs maps obtained at the time of fracture are shown in Figures 27(ⅰ-c-2) and (ⅱ-c-2). Here, the GNDs primarily concentrate in the columnar grain zones and exhibit the band distribution characteristics directly related to the heterogeneous structure of the WAAM-processed 2219 Al alloy deposit. Compared with the equiaxed grains, columnar grains undergo larger deformation and possess a stronger ability to coordinate the deformation process.

The IPF and GND maps of the WC and AC deposits obtained after tensile testing along the vertical direction are shown in Figures 27(ⅲ) and (ⅳ), respectively. At EL = 5% (Figure 27(ⅲ-b-2)), the dislocations were first concentrated in the columnar grain zones. When the fracture occurred, many dislocations were present in all columnar grains, and a large GND value was obtained at the grain boundary. Meanwhile, the equiaxed grain zone still exhibited low GNDs (Figure 27(ⅲ-c-2)). For the AC deposit, the GND change trend was similar to that of the WC deposit. The coordinated

deformation between the crystal grains became relatively uniform only after the fracture. These observations indicate that the difference between the structures of the columnar and equiaxed grains plays a significant role in enhancing alloy's ductility.

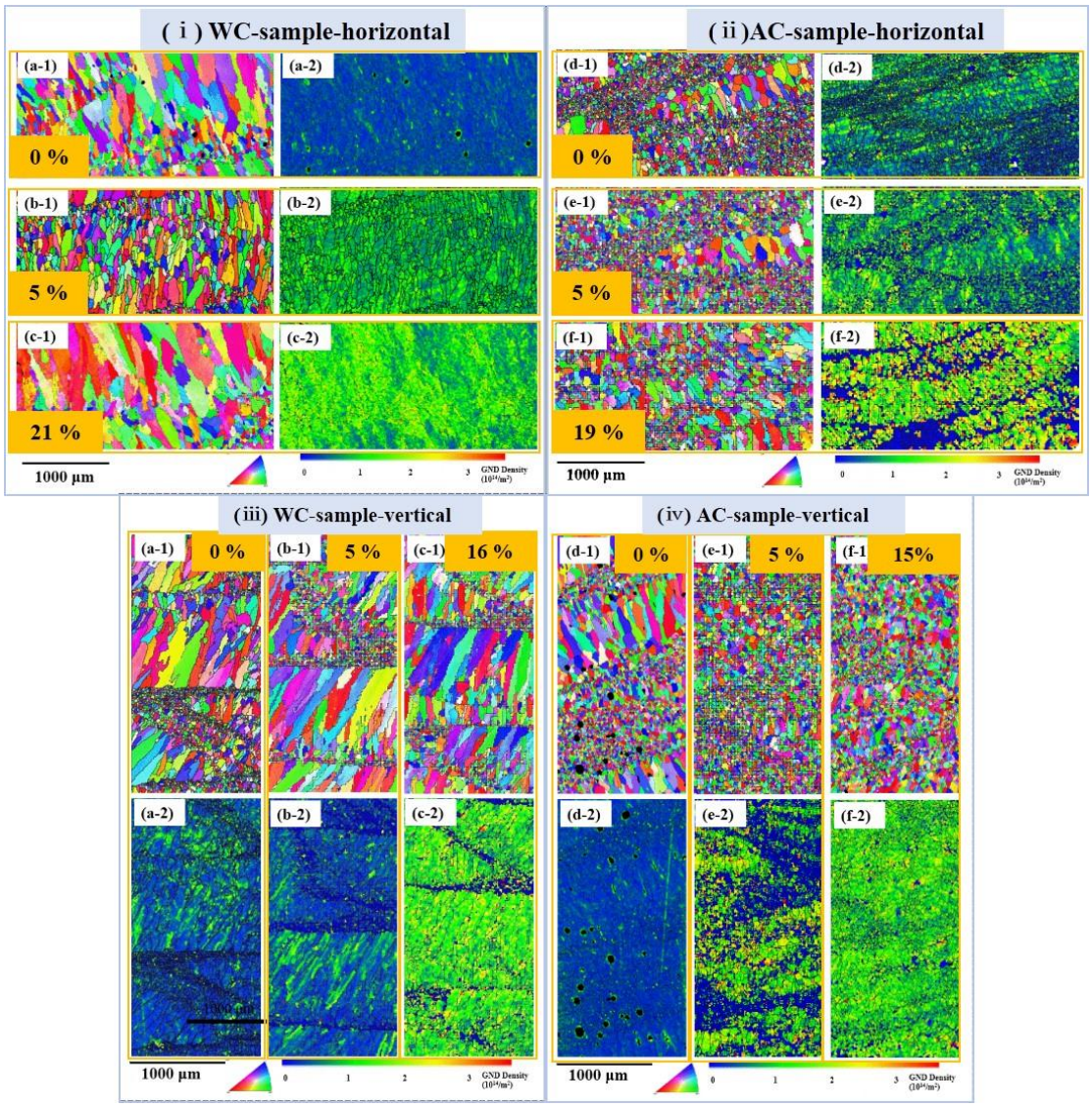

Figure 27 The IPF (x-1) and GND maps (x-2) for the WAAM-processed 2219 Al with different deformation amount during tension test: (i) WC deposit along horizontal direction: (a-x) strain 0%; (b-x) strain 5%; (c-x) fracture; (ii) AC deposit along horizontal direction; (iii) WC deposit along vertical direction; (iv) AC deposit along vertical direction.

A typical microstructure of the WAAM-processed 2219 Al alloy is a heterogeneous band structure, which can achieve good strength-ductility synergy [18, 57]. A schematic diagram of the deformation mechanism in the WAAM-processed 2219 Al deposit is shown in Figure 28. Here, the heterogeneous structure is characterized by a combination of the soft columnar grain zone and hard equiaxed grain zone. The

deformation of the heterogeneous structure is mainly divided into three stages [29, 31]. At stage I, both the equiaxed and columnar grain zones deform elastically. During stage Ⅱ, the columnar grain zone begins to deform plastically, and the equiaxed grain zone remains in the elastic deformation mode. At stage III, both the equiaxed and columnar grains undergo plastic deformation. The columnar grain zone is more plastically deformed than the equiaxed grain, resulting in a relatively uniform strain distribution (the columnar grains become elongated, but the equiaxed grains remain intact). Owing to the limitation of the equiaxed grain region, the soft region cannot deform freely. A strain gradient is generated at the interface near the columnar grain region, which can adjust the strain gradient to maintain the coordinated deformation of the equiaxed grain and columnar grain regions [30]. The pile-up of GNDs produces a long-range internal stress or back stress, which inhibits the movement of dislocations in the columnar grain region to strengthen the columnar grain region and ultimately increases the YS value. The accumulation of GNDs generates not only a back stress in the columnar grain region, but also stress concentration at the interface. Therefore, the equiaxed grain region produces normal stress to coordinate the stress concentration. A combination of back stress and normal stress is generally called hetero-deformation-induced hardening [29]. During tensile deformation, the equiaxed grain constrains the deformation of columnar grains, leading to the generation of GNDs at the band interface.

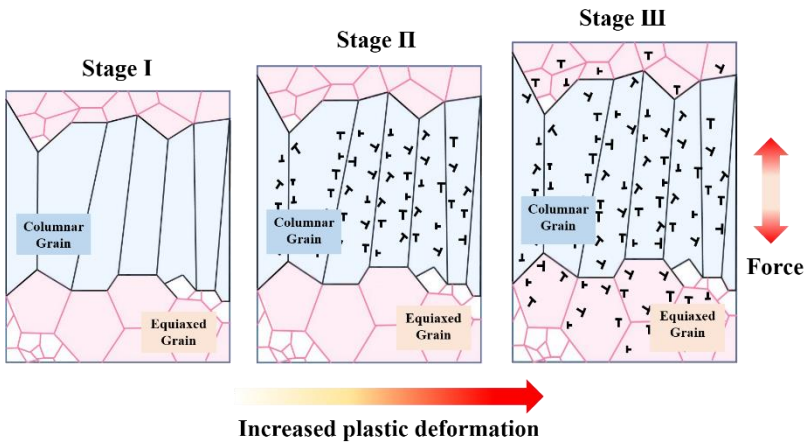

Figure 28 The schematic representation of the plastic deformation stages of the WAAM-processed 2219 Al alloy with the WC condition.

5. Conclusions

In this study, the heterogeneous band structure in the WAAM-processed 2219 Al alloy was obtained by varying the cooling mode of the substrate. The following conclusions were drawn from its findings:

(1) According to the CET theory, the formation of equiaxed grains at the molten pool boundaries is attributed to the increase in N_0 caused by the precipitation of Al_3Zr particles during solidification. However, the precipitation of Al_3Zr particles in the molten pool is limited by the cooling rate, and the equiaxed grains are gradually transformed into columnar grains.

(2) The pores are mainly concentrated in the interlayer equiaxed grains zone. Both the computational and experimental data show that the porosity and pore size of WC deposit are smaller than those of the AC deposit.

(3) The heterogeneous band structure can be divided into the soft columnar grain zone with a hardness of 76 HV and hard equiaxed grain zone with a hardness of 86 HV. The UTS, YS, and EL values of the WC deposit with a columnar grain ratio of 85% are 10.76%, 15.78%, and 26.78% higher than those of the AC deposit with a columnar grain ratio of 69%, respectively.

(4) The stress-strain curve exhibits an apparent PLC effect. During the deformation of the heterogeneous band structure of the WAAM-processed 2219 Al alloy, the soft columnar grain zone coordinates plastic deformation first and thus possesses better coordinated deformation ability than that of the hard equiaxed zone to achieve good strength-ductility synergy.

Acknowledgements

The authors gratefully acknowledge the financial support of the project from the Advance Research Projects in the Field of Manned Spaceflight (Project No. 040302) and Shanghai Aerospace Science and Technology Innovation Fund Project (Project No. SAST2018-066).

CRediT authorship contribution statement

Yinghui Zhou: Investigation, Data curation, Methodology, Writing - original draft

Xin Lin: Funding acquisition, Project administration, Resources, Supervision Validation, Writing - review & editing

Nan Kang: Writing - review & editing, Supervision

Yao Tang: Thermal simulation investigation

Weidong Huang: Funding acquisition, Resources

Zhennan Wang: Investigation

Declaration of Competing Interest

The authors declare that they have no known competing financial interests or personal relationships that could have appeared to influence the work reported in this paper.

References

[1] H. Miyoshi, H. Kimizuka, A. Ishii, S. Ogata, Temperature-dependent nucleation kinetics of Guinier-Preston zones in Al–Cu alloys: An atomistic kinetic Monte Carlo and classical nucleation theory approach, Acta Materialia 179 (2019) 262-272.

[2] J. Gu, S. Yang, M. Gao, J. Bai, K. Liu, Influence of deposition strategy of structural interface on microstructures and mechanical properties of additively manufactured Al alloy, Additive Manufacturing 34 (2020) 101370.

[3] H.L. Wei, J.W. Elmer, T. DebRoy, Three-dimensional modeling of grain structure evolution during welding of an aluminum alloy, Acta Materialia 126 (2017) 413-425.

[4] T. DebRoy, H.L. Wei, J.S. Zuback, T. Mukherjee, J.W. Elmer, J.O. Milewski, A.M. Beese, A. Wilson-Heid, A. De, W. Zhang, Additive manufacturing of metallic components-Process, structure and properties, Progress in Materials Science 92 (2018) 112-224.

[5] C. Jia, W. Liu, M. Chen, M. Guo, S. Wu, C. Wu, Investigation on arc plasma, droplet, and molten pool behaviours in compulsively constricted WAAM, Additive Manufacturing 34 (2020) 101235.

[6] Y. Fu, H. Zhang, G. Wang, H. Wang, Investigation of mechanical properties for hybrid deposition and micro-rolling of bainite steel, Journal of Materials Processing Technology 250 (2017) 220-227.

[7] J. Gu, S. Yang, M. Gao, J. Bai, Y. Zhai, J. Ding, Micropore evolution in additively manufactured aluminum alloys under heat treatment and inter-layer rolling, Materials & Design 186 (2020) 108288.

[8] J. Gu, J. Ding, S.W. Williams, H. Gu, J. Bai, Y. Zhai, P. Ma, The strengthening effect of inter-layer cold working and post-deposition heat treatment on the additively manufactured Al–6.3Cu alloy, Materials Science & Engineering: A 651 (2016) 18-26.

[9] Z. Wang, X. Lin, L. Wang, Y. Cao, Y. Zhou, W. Huang, Microstructure evolution and mechanical properties of the wire + arc additive manufacutring Al-Cu alloy, Additive Manufacturing 47 (2021) 102298.

[10] C. Zhang, Y. Li, M. Gao, X. Zeng, Wire arc additive manufacturing of Al-6Mg alloy using variable polarity cold metal transfer arc as power source, Materials Science & Engineering: A 711 (2018) 415-423.

[11] J. Gu, J. Ding, S.W. Williams, H. Gu, P. Ma, Y. Zhai, The effect of inter-layer cold working and post-deposition heat treatment on porosity in additively manufactured aluminum alloys, Journal of Materials Processing Technology 230 (2016) 26-34.

[12] Z. Qi, B. Cong, B. Qi, H. Sun, G. Zhao, J. Ding, Microstructure and mechanical properties of double-wire + arc additively manufactured Al-Cu-Mg alloys, Journal of Materials Processing Technology 255 (2018) 347-353.

[13] J. Gu, X. Wang, J. Bai, J. Ding, S. Williams, Y. Zhai, K. Liu, Deformation microstructures and

strengthening mechanisms for the wire+arc additively manufactured Al-Mg4.5Mn alloy with inter-layer rolling, Materials Science & Engineering: A 712 (2018) 292-301.

[14] J.Y. Bai, C.L. Fan, S.B. Lin, C.L. Yang, B.L. Dong, Mechanical properties and fracture behaviors of GTA-additive manufactured 2219-Al after an especial heat treatment, Journal of Materials Engineering and Performance 26(4) (2017) 1808-1816.

[15] Y. Xu, D. Casari, R.H. Mathiesen, Y. Li, Revealing the heterogeneous nucleation behavior of equiaxed grains of inoculated Al alloys during directional solidification, Acta Materialia 149 (2018) 312-325.

[16] C.Y. Wang, C. Beckermann, Prediction of columnar to equiaxed transition during diffusion-controlled dendritic alloy solidification, Metallurgical and materials transactions A 25A (1994) 1081-1093.

[17] D.A. Porter, K.E. Easterling, M.Y. Sherif, Phase Transformations in Metals and Alloys, Third edition CRC Press, 2009.

[18] Z. Wang, X. Lin, N. Kang, Y. Hu, J. Chen, W. Huang, Strength-ductility synergy of selective laser melted Al-Mg-Sc-Zr alloy with a heterogeneous grain structure, Additive Manufacturing 34 (2020) 101260.

[19] S. Hori, S. Saji, A. Takehara, Metastable phase and grain refinement in rapidly sodilified Al-Zr alloys, Journal of Japan Institute of Light Metals 31 (1981) 793-797.

[20] K.V. Yang, Y. Shi, F. Palm, X. Wu, P. Rometsch, Columnar to equiaxed transition in Al-Mg(-Sc)-Zr alloys produced by selective laser melting, Scripta Materialia 145 (2018) 113-117.

[21] A. Gutierrez, J.C. Lippold, A proposed mechanism for equiaxed grain formation along the fusion boundary in aluminum-copper-lithium alloys, Welding Journal 77 (1998) 122-132.

[22] D.C. Lin, G.-X. Wang, T.S. Srivatsan, A mechanism for the formation of equiaxed grains in welds of aluminum-lithium alloy 2090, Materials Science & Engineeing: A 351 (2003) 304-309.

[23] A. Gutierrez, J.C. Lippold, W. Lin, Nondendritic equiaxed zone formation in aluminum-lithium welds, Materials Science Forum 217-222 (1996) 1691-1696.

[24] Y. Li, D. Gu, Parametric analysis of thermal behavior during selective laser melting additive manufacturing of aluminum alloy powder, Materials & Design 63 (2014) 856-867.

[25] R. Geng, J. Du, Z. Wei, S. Xu, N. Ma, Modelling and experimental observation of the deposition geometry and microstructure evolution of aluminum alloy fabricated by wire-arc additive manufacturing, Journal of Manufacturing Processes 64 (2021) 369-378.

[26] Z. Zhang, C. Sun, X. Xu, L. Liu, Surface quality and forming characteristics of thin-wall aluminium alloy parts manufactrued by laser assisted MIG arc additvie manufacturing, International Journal of Lightweight Materials and Manufacture 1 (2018) 89-95.

[27] J. Yang, J. Han, H. Yu, J. Yin, M. Gao, Z. Wang, X. Zeng, Role of molten pool mode on formability, microstructure and mechanical properties of selective laser melted Ti-6Al-4V alloy, Materials & Design 110 (2016) 558-570.

[28] X. Wu, M. Yang, F. Yuan, G. Wu, Y. Wei, X. Huang, Y. Zhu, Heterogeneous lamella structure unites ultrafine-grain strength with coarse-grain ductility, Proceedings of the National Academy of Sciences 112(47) (2015) 14501-14505.

[29] Y. Zhu, X. Wu, Perspective on hetero-deformation induced (HDI) hardening and back stress, Materials Research Letters 7(10) (2019) 393-398.

[30] Z.K. Li, X.T. Fang, Y.F. Wang, P. Jiang, J.J. Wang, C.M. Liu, X.L. Wu, Y.T. Zhu, C.C. Koch, Tuning heterostructures with powder metallurgy for high synergistic strengthening and hetero-deformation induced hardening, Materials Science and Engineering: A 777 (2020) 139074.

[31] P. Sathiyamoorthi, H.S. Kim, High-entropy alloys with heterogeneous microstructure: Processing and mechanical properties, Progress in Materials Science 123 (2020) 100709.

[32] Z. Wang, X. Lin, Y. Tang, N. Kang, X. Gao, S. Shi, W. Huang, Laser-based directed energy deposition of novel Sc/Zr-modified Al-Mg alloys: columar-to-equiaxed transition and aging hardening behavior, Journal of Materials Science & Technology 69 (2021) 168-179.

[33] Z. Hu, Y. Qi, X. Nie, H. Zhang, H. Zhu, The Portevin-Le Chatelier (PLC) effect in an Al-Cu aluminum alloy fabricated by selective laser melting Materials Characerization 178 (2021) 111198.

[34] M. Ma, Z. Wang, X. Zeng, A comparison on metallurgical behaviors of 316L stainless steel by selective laser melting and laser cladding deposition, Materials Science & Engineeing: A 685 (2017) 265-273.

[35] H. Jacobi, K. Schwerdtfeger, Dendrite morphology of steady state unidirectionally solidified steel, Metallurgical Transactions A 7A (1976) 811-820.

[36] X. Lin, W. Huang, J. Feng, T. Li, Y. Zhou, History-dependent selection of primary cellular/dendritic spacing during unidirectional solidification in aluminum alloys, Acta Materialia 47 (1999) 3271-3280.

[37] M. Gäumann, Cle′ton, F, J.-D. Wagnie`re, W. Kurz, Epitaxial laser metal forming: analysis of microsturcture formation, Materials science & Engineeing: A 271 (1999) 232-241.

[38] M. Chiumenti, X. Lin, M. Cervera, L. Wei, Y. Zheng, W. Huang, Numerical simulation and experimental calibration of additive manufacturing by blown powder technology. Part I: thermal analysis, Rapid Prototyping Journal 23(2) (2017) 448-463.

[39] C. Liu, J. He, Numerical analysis of thermal fluid transport behavior during electron beam welding of 2219 aluminum alloy plate, Transactions of Nonferrous Metals Society of China 27(6) (2017) 1319-1326.

[40] Y. Zhou, X. Lin, N. Kang, W. Huang, Z. Wang, Mechanical properties and precipitation behavior of

the heat-treated wire + arc additively manufactured 2219 aluminum alloy, Materials Characerization 171 (2021) 110735.

[41] M. Opprecht, J.-P. Garandet, G. Roux, C. Flament, An understanding of duplex microstructures encountered during high strength aluminium alloy laser beam melting processing, Acta Materialia 215 (2021) 117024.

[42] Q. Tan, J. Zhang, Q. Sun, Z. Fan, G. Li, Y. Yin, Y. Liu, Inoculation treatment of an additively manufactured 2024 aluminium alloy with titanium nanoparticles, Acta Materialia 196 (2020) 1-16.

[43] Y.L. Cai, S.L. Yang, Y.H. Wang, S.H. Fu, Q.C. Zhang, Characterization of the deformation behaviors associated with the serrated flow of a 5456 Al-based alloy using two orthogonal digital image correlation systems, Materials Science & Engineering: A 664 (2016) 155-164.

[44] W. Kurz, D.J. Fisher, Dendrite growth at the limit of stability: tip radius and spacing, Acta Materialia 29 (1981) 11-20.

[45] J.D. Hunt, Steady state columnar and equiaxed growth of dendrites and eutectic, Materials Science & Engineeing 65 (1984) 75-83.

[46] M. Gäumann, C. Bezencon, P. Canalis, W. Kurz, Single-crystal laser depostion of superalloys: processing-microstructure maps, Acta Materialia 49(6) (2001) 2268-2273.

[47] B.L. Dong, P.D. Lee, Simulation of the columnar-to-equiaxed transition in directionally solidified Al–Cu alloys, Acta Materialia 53 (2005) 659-668.

[48] A.E. Ares, S.F. Gueijman, C.E. Schvezov, An experimental investigation of the columnar-to-equiaxed grain transition in aluminum–copper hypoeutectic and eutectic alloys, Journal of Crystal Growth 312(14) (2010) 2154-2170.

[49] D.G. McCartney, Grain refining of aluminium and its alloys using inoculants, International Materials Reviews 34 (2013) 247-260.

[50] M.A. Martorano, C. Beckermann, C.-A. Gandin, A solutal interaction mechanism for the columnar-to-equiaxed transition in alloy solidification, Metallurgical and materials transactions A 34A (2003) 1657-1674.

[51] M. Opprecht, J.-P. Garandet, G. Roux, C. Flament, M. Soulier, A solution to the hot cracking problem for aluminium alloys manufactured by laser beam melting, Acta Materialia 197 (2020) 40-53.

[52] C. Chen, M. Gao, H. Mu, X. Zeng, Effect of kerf characteristics on weld porosity of laser cutting-welding of AA2219 aluminum alloy, Applied Surface Science 494 (2019) 1036-1043.

[53] J.C. Stinville, M.A. Charpagne, F. Bourdin, P.G. Callahan, Z. Chen, M.P. Echlin, D. Texier, J. Cormier, P. Villechaise, T.M. Pollock, V. Valle, Measurement of elastic and rotation fields during irreversible deformation using Heaviside-digital image correlation, Materials Characterization 169 (2020) 110600.

[54] P. Li, H. Li, L. Huang, X. Liang, Z. Zhu, Characterization of hot deformation behavior of AA2014 forging aluminum alloy using processing map, Transactions of Nonferrous Metals Society of China 27(8) (2017) 1677-1688.

[55] H. Gao, Y. Huang, W.D. Nix, J.W. Hutchinson, Mechanism-based strain gradient plasticity-I. Theory, Journal of the Mechanics and Physics of Solids 47 (1999) 1239-1263.

[56] L.O. Kubin, A. Mortensen, Geometrically necessary dislocations and strain-gradient plasticity: a few critical issues, Scripta Materialia 48 (2003) 119-125.

[57] Z. Wang, X. Lin, N. Kang, J. Chen, Y. Tang, H. Tan, X. Yu, H. Yang, W. Huang, Directed energy deposition additive manufacturing of a Sc/Zr-modified Al-Mg alloy: Effect of thermal history on microstructural evolution and mechanical properties, Materials Science & Engineeing: A 802 (2021) 140606.